

Decipher the R_{Ψ_m} correlator in search for the chiral magnetic effect in relativistic heavy ion collisions

Yicheng Feng,^{1,*} Jie Zhao,^{1,†} Hao-jie Xu,^{2,‡} and Fuqiang Wang^{1,2,§}

¹*Department of Physics and Astronomy, Purdue University, West Lafayette, IN 47907, USA*

²*School of Science, Huzhou University, Huzhou, Zhejiang 313000, China*

(Dated: April 2, 2021)

Background: The chiral magnetic effect (CME) is extensively studied in heavy-ion collisions at RHIC and the LHC. An azimuthal correlator called R_{Ψ_m} was proposed to measure the CME. By observing the same R_{Ψ_2} and R_{Ψ_3} (convex) distributions from A Multi-Phase Transport (AMPT) model, by contrasting data and model as well as large and small systems and by event shape engineering (ESE), a recent preprint (arXiv:2006.04251v1) from STAR suggests that the R_{Ψ_m} observable is sensitive to the CME signal and relatively insensitive to backgrounds, and their Au+Au data are inconsistent with known background contributions.

Purpose: We examine those claims by studying the robustness of the R_{Ψ_m} observable using AMPT as well as toy model simulations. We compare R_{Ψ_m} to the more widely used $\Delta\gamma$ azimuthal correlator to identify their commonalities and differences.

Methods: We use AMPT to simulate Au+Au, p+Au, and d+Au collisions at $\sqrt{s_{NN}} = 200$ GeV, and study the responses of R_{Ψ_m} to anisotropic flow backgrounds in the model. We also use a toy model to simulate resonance flow background and input CME signal to investigate their effects in R_{Ψ_2} . Additionally we use the toy model to perform an ESE analysis to compare to STAR data as well as predict the degree of sensitivity of R_{Ψ_2} to isobar collisions with the event statistics taken at RHIC.

Results: Our AMPT results show that the R_{Ψ_2} in Au+Au collisions is concave and apparently different from R_{Ψ_3} , in contradiction to the findings in STAR's preprint, while the R_{Ψ_2} in p+Au and d+Au collisions are slightly concave. Our toy model ESE analysis indicates that the R_{Ψ_2} is sensitive to the event-by-event anisotropy q_2 as well as the elliptic flow parameter v_2 . The toy model results further show that R_{Ψ_2} depends on both the CME signal and the flow backgrounds, similar to the $\Delta\gamma$ observable. It is found that the R_{Ψ_2} and $\Delta\gamma$ observables show similar sensitivities and centrality dependences in isobar collisions.

Conclusions: Our AMPT results contradict those from a recent preprint by STAR. Our toy model simulations demonstrate that R_{Ψ_2} is sensitive to both the CME signal and physics backgrounds. Toy model simulations of isobar collisions show similar centrality dependence and magnitudes for the relative R_{Ψ_2} strengths as well as the relative $\Delta\gamma$ strengths. We conclude that R_{Ψ_2} and the inclusive $\Delta\gamma$ are essentially the same.

PACS numbers: 25.75.-q, 25.75.Gz, 25.75.Ld

1. INTRODUCTION

In quantum chromodynamics (QCD), topological charge fluctuations in vacuum can cause chiral anomaly in local domains [1–4]. Such domains violate the parity (\mathcal{P}) and charge-parity (\mathcal{CP}) symmetry. If a strong enough external magnetic field is also present, quark spins would be locked depending on their charge, either parallel or anti-parallel to the magnetic field. As a result, charge separation along the magnetic field would emerge in those chirality imbalanced domains, which has observational consequences in the final state. This is called the chiral magnetic effect (CME) [3, 4].

In non-central heavy ion collisions, excited QCD vacuum is formed in the central collision zone, whereas the spectator protons can provide an intense, transient magnetic field [4]. Thus, the CME is expected to emerge in

those collisions, which, if observed, would be a strong evidence for local \mathcal{P} and \mathcal{CP} violation in the strong interaction.

The magnetic field created in heavy-ion collisions is, on average, perpendicular to the reaction plane (RP, spanned by the impact parameter and the beam direction). A RP-dependent charge correlation observable $\Delta\gamma$ has been proposed [5] and widely studied at the Relativistic Heavy Ion Collider (RHIC) [6–11] and the Large Hadron Collider (LHC) [12–16]. An alternate correlator, called R_{Ψ_m} ($m = 2$ or 3 is the azimuthal harmonic order), was also proposed [17, 18]. The premise was that the physics backgrounds should result in a convex R_{Ψ_2} distribution and the CME signal should give a concave one. This was contradicted by other background studies [19], including one by us [20].

Recently, the STAR collaboration released results [21] using a modified R_{Ψ_2} variable (see Sec. 2.1). Their AMPT (a multiphase transport [22]) and AVFD (Anomalous Viscous Fluid Dynamics [23, 24]) model studies, suggest that R_{Ψ_2} is sensitive to the CME signal and relatively insensitive to backgrounds. It is found that the AMPT R_{Ψ_m} results are convex and equal between R_{Ψ_2} and R_{Ψ_3} ; that the R_{Ψ_2} in Au+Au collisions is concave

* feng216@purdue.edu

† zhao656@purdue.edu

‡ haojiexu@zjhu.edu.cn

§ fqwang@purdue.edu

and in p+Au and d+Au collisions are flat or convex; and that the R_{Ψ_2} distribution in an event shape engineering (ESE) [25] analysis is insensitive to the event-by-event anisotropy parameter which is in turn sensitive to the flow anisotropy. These findings led to the conclusion that the Au+Au data indicate a strong signal consistent with the CME that cannot be explained by known backgrounds.

Since the qualitative features of the AMPT results by STAR [21] contradict the other similar background studies [19, 20], further investigations are warranted. In this paper, we first revisit our earlier AMPT study using the modified R_{Ψ_m} variable [18] that was employed by STAR [21]. We also investigate small system collisions simulated by AMPT. We then perform an ESE analysis using a toy model simulation in order to have sufficient statistics. We further examine the R_{Ψ_2} variable with the toy model, investigating its effectiveness to identify the input CME signal and its vulnerability to physics backgrounds, in an attempt to decipher the R_{Ψ_m} variable. We discuss our findings in the context of the STAR results [21].

The rest of the article is organized as follows. In Sec. 2, the definitions of R_{Ψ_m} and $\Delta\gamma$ are provided. In Sec. 3, AMPT simulation results on R_{Ψ_m} are presented in Au+Au, p+Au, and d+Au collisions. In Sec. 4, an ESE study is conducted using toy model simulations. In Sec. 5, the toy model is used to study the elliptic flow (v_2) background and the CME signal (a_1) dependences for both R_{Ψ_2} and $\Delta\gamma$ in Au+Au and isobar collisions. In Sec. 6, a summary is given. Appendix A gives an analytical derivation for the event-plane resolution correction and discusses further complications. In Appendix B, we extend our analytical analysis in Ref. [20] to the modified R_{Ψ_2} variable for the pure background case, and derive an analytical form for the CME signal dependence of the R_{Ψ_2} variable. In Appendix C, we also provide an analytical form for the signal and background dependence of $\Delta\gamma$.

2. METHODOLOGY

2.1. The R_{Ψ_m} correlator

Phenomenologically, the azimuthal distribution of the primordial particles in each event can be expressed into Fourier expansion

$$\frac{dN^\pm}{d\phi} \propto 1 \pm 2a_1 \sin(\phi - \Psi_{\text{RP}}) + 2v_2 \cos 2(\phi - \Psi_{\text{RP}}) + \dots, \quad (1)$$

where Ψ_{RP} denotes the RP azimuthal angle. The N^\pm is the number of particles with charge sign indicated by its superscript. The coefficient $\pm a_1$ is the charge-dependent CME signal, and v_2 is the elliptic flow coefficient. In real data analysis, the RP is often surrogated by the second-order event plane (EP). The azimuthal angle of the EP

of the order m is calculated by

$$\Psi_m = \frac{1}{m} \arctan \left(\frac{\sum_i w_i \sin(m\phi_i)}{\sum_i w_i \cos(m\phi_i)} \right), \quad (2)$$

where ϕ_i and w_i are the azimuthal angle and weight of particle i .

To avoid auto-correlations, the particles of interests (POI, whose azimuth is ϕ) to measure the CME (or the a_1 parameter) must be excluded from the particles used to reconstruct the EP. To realize that, the subevent method is used to define the R_{Ψ_m} correlator. Each event is divided into two subevents with a pseudorapidity gap – one subevent (referred to as “east” subevent) with $-1.0 < \eta < -0.1$ and the other (referred to as “west” subevent) with $0.1 < \eta < 1.0$. We take the west subevent as an example to calculate the charge separation perpendicular to the east-subevent EP (ΔS^W) and parallel to it ($\Delta S^{\perp,W}$), according to the real charge sign. Namely,

$$\begin{aligned} \Delta S_m^W &= \frac{1}{n_W^+} \sum_{i \in W}^{n_W^+} \sin \left(\frac{m}{2} (\phi_i^+ - \Psi_m^E) \right) \\ &\quad - \frac{1}{n_W^-} \sum_{i \in W}^{n_W^-} \sin \left(\frac{m}{2} (\phi_i^- - \Psi_m^E) \right), \\ \Delta S_m^{\perp,W} &= \frac{1}{n_W^+} \sum_{i \in W}^{n_W^+} \sin \left(\frac{m}{2} (\phi_i^+ - \Psi_m^E) + \frac{\pi}{2} \right) \\ &\quad - \frac{1}{n_W^-} \sum_{i \in W}^{n_W^-} \sin \left(\frac{m}{2} (\phi_i^- - \Psi_m^E) + \frac{\pi}{2} \right). \end{aligned} \quad (3)$$

To combine the two subevents, we take the average

$$\begin{aligned} \Delta S_m &= (\Delta S_m^W + \Delta S_m^E) / 2, \\ \Delta S_m^\perp &= (\Delta S_m^{\perp,W} + \Delta S_m^{\perp,E}) / 2. \end{aligned} \quad (4)$$

The widths of the distributions in ΔS_m characterize the magnitude of charge separation with respect to the plane with which the ΔS_m is defined. The widths depend on the multiplicity of particles used to compute the ΔS_m . To normalize out the multiplicity dependence, reference variables $\Delta S_{m,\text{sh}}$ and $\Delta S_{m,\text{sh}}^\perp$ are constructed by randomly shuffling the particle charge signs (according to relative abundances of positive and negative particles). Denoting $\sigma_{m,\text{sh}}$ and $\sigma_{m,\text{sh}}^\perp$ for the RMS widths of the shuffled distributions, the ΔS_m variables are scaled as follows [21],

$$\Delta S'_m = \Delta S_m / \sigma_{m,\text{sh}}, \quad \Delta S'^\perp_m = \Delta S_m^\perp / \sigma_{m,\text{sh}}^\perp. \quad (5)$$

Because of finite multiplicity fluctuations, the reconstructed EP is smeared from the RP, broadening the ΔS_m distributions. A multiplicative factor is applied to correct for the effect of the imperfect EP reconstruction,

$$\Delta S''_m = \Delta S'_m \delta_{r_m}, \quad \Delta S''^\perp_m = \Delta S'^\perp_m \delta_{r_m}. \quad (6)$$

The correction factor is given by

$$\delta_{r_m} = \sqrt{r_m}, \quad (7)$$

where r_m is the EP resolution of subevents,

$$r_m = \langle \cos m(\Psi_m^{E/W} - \Psi_{\text{RP}}) \rangle = \sqrt{\langle \cos m(\Psi_m^W - \Psi_m^E) \rangle}. \quad (8)$$

The derivation of Eq. 7 is given in Appendix A.1.

The normalized distributions of $\Delta S''_m$ are

$$C_{\Psi_m} = \frac{\text{event probability distribution in } \Delta S''_m}{\text{event probability distribution in } \Delta S''_{m,\text{sh}}}, \quad (9)$$

$$C_{\Psi_m}^\perp = \frac{\text{event probability distribution in } \Delta S''_{m,\text{sh}}^\perp}{\text{event probability distribution in } \Delta S''_{m,\text{sh}}^\perp}.$$

The R_{Ψ_m} observable is defined by the double ratio

$$R_{\Psi_m} = \frac{C_{\Psi_m}}{C_{\Psi_m}^\perp}. \quad (10)$$

We characterize the shape of R_{Ψ_m} by

$$\xi = -\frac{1}{\delta_{r_m}^2} \left(\frac{\sigma_{m,\text{sh}}^2}{\sigma_m^2} - \frac{\sigma_{m,\text{sh}}^{\perp 2}}{\sigma_m^{\perp 2}} \right). \quad (11)$$

The variable ξ can also be obtained by fitting the R_{Ψ_m} distributions to $Ce^{\xi x^2/2}$. The distribution of R_{Ψ_m} is concave when $\xi > 0$, convex when $\xi < 0$, and flat when $\xi = 0$. The width of R_{Ψ_m} is $\sigma = 1/\sqrt{|\xi|}$, so we will refer to ξ as the squared inverse width of R_{Ψ_m} .

As will be discussed in Section 5.1, the averaging of Eq. 4 introduces auto-correlations and is thus not a good way to define ΔS_m and ΔS_m^\perp . We propose not to average the two subevents but treat them separately. See Section 5.1 and Appendix A for more details. Nonetheless, for comparisons to the previous works, we study both cases where the subevents are averaged as well as treated independently, and use the same correction factor given by Eq. 7.

2.2. The $\Delta\gamma$ observable

The two-particle azimuthal correlator $\Delta\gamma$ observable [5] is widely used in CME studies at RHIC [6–11] and the LHC [12–16]. For completeness, we give a brief description of the $\Delta\gamma$ observable. To keep consistency with the R_{Ψ_m} , we define $\Delta\gamma$ also by subevents,

$$\gamma_{\text{OS}} = \langle \cos(\phi_{a \in E/W}^\pm + \phi_{b \in E/W}^\mp - 2\Psi_2^{W/E}) \rangle / r_2,$$

$$\gamma_{\text{SS}} = \langle \cos(\phi_{a \in E/W}^\pm + \phi_{b \in E/W}^\pm - 2\Psi_2^{W/E}) \rangle / r_2, \quad (12)$$

$$\Delta\gamma = \gamma_{\text{OS}} - \gamma_{\text{SS}},$$

where a and b are two particles in the same subevent and r_2 is the second-order EP resolution of the subevents, as

in Eq. 8. In order to compare with R_{Ψ_2} , the same POI cuts and EP particle cuts as in R_{Ψ_2} are used in $\Delta\gamma$.

For the CME signal parameterized by the a_1 parameter in Eq. 1, the $\Delta\gamma$ correlator can be obtained as

$$\Delta\gamma = 2a_1^2. \quad (13)$$

It is well known that $\Delta\gamma$ is strongly contaminated by physics backgrounds caused by two-particle correlations and the anisotropy of those correlated pairs [5, 26–29]. For instance, resonance decays present a major background:

$$\Delta\gamma = \frac{N_{\text{reso}}}{N_{\text{pair}}} \langle \cos(\phi_a + \phi_b - 2\phi_{\text{reso}}) \rangle v_{2,\text{reso}}. \quad (14)$$

Since the number of resonances $N_{\text{reso}} \propto N$, the number of pairs $N_{\text{pair}} \propto N^2$, and the resonance elliptic flow $v_{2,\text{reso}} \propto v_2$, the background contamination in $\Delta\gamma$ is generally proportional to the final-state particle v_2 and inversely proportional to the multiplicity (N).

3. AMPT RESULTS

The AMPT model [22] is widely used to simulate relativistic heavy ion collisions, without CME signal. In this study, we use the AMPT version v2.25t4cu2 where charge conservation is ensured. We set the model parameter NTMAX=150 which means that the hadronic cascade is turned on. For particles used for EP reconstruction, a cut is applied to their transverse momentum $0.2 \text{ GeV}/c < p_T < 2.0 \text{ GeV}/c$, while for POI, a tighter p_T cut is applied $0.35 \text{ GeV}/c < p_T < 2.0 \text{ GeV}/c$, as in the STAR analysis [21]. All particles used in our analysis are required to be inside the η range $-1 < \eta < 1$.

3.1. Au+Au collisions

For Au+Au collisions at $\sqrt{s_{NN}} = 200 \text{ GeV}$, the minimal bias (MB) AMPT events are generated first to define centrality by cutting on MB multiplicity distribution. Then, a total of 25.8 million 30–50% centrality events are simulated and used for this analysis. Figure 1 shows the R_{Ψ_2} (red square) and R_{Ψ_3} (blue circle) distributions. The distributions are concave and different from each other in width. This is in stark contrast to the STAR results in Ref. [21], where convex, nearly-identical R_{Ψ_2} and R_{Ψ_3} curves were obtained. The “identical” R_{Ψ_2} and R_{Ψ_3} curves from AMPT (where only backgrounds are present, with no CME signal) was critical for the claim in Ref. [21] that the Au+Au data, where different R_{Ψ_2} and R_{Ψ_3} distributions are observed, are consistent with CME and inconsistent with known backgrounds. Since the v_2 and v_3 physics mechanisms are the same in the hydrodynamic picture, it may be satisfactory to find identical R_{Ψ_2} and R_{Ψ_3} curves. However, our AMPT results

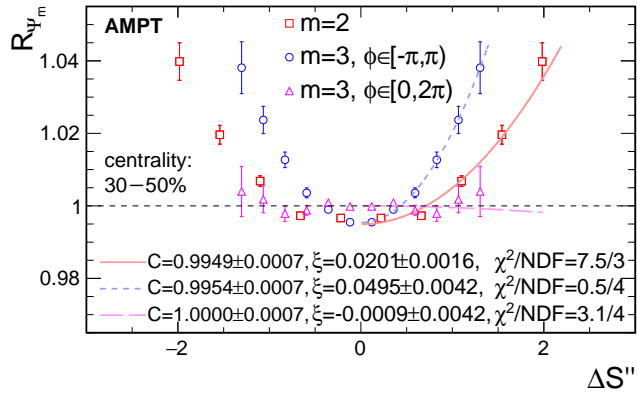


FIG. 1. The R_{Ψ_2} and R_{Ψ_3} distributions in centrality 30–50% Au+Au collisions at $\sqrt{s_{NN}} = 200$ GeV simulated by AMPT. Total 25.8 million 30–50% centrality events are generated and analyzed. The POI are required to have $0.35 \text{ GeV}/c < p_T < 2.0 \text{ GeV}/c$ and $0.1 < |\eta| < 1.0$, whereas particles used for EP reconstruction are required to have $0.2 \text{ GeV}/c < p_T < 2.0 \text{ GeV}/c$ and $0.1 < |\eta| < 1.0$. The R_{Ψ_m} distributions are symmetrized. With the azimuth range $\phi \in [-\pi, \pi)$, the R_{Ψ_2} (red square) and R_{Ψ_3} (blue circle) curves are both concave and apparently different. With the range $\phi \in [0, 2\pi)$, R_{Ψ_3} (magenta triangle) is relatively flat and R_{Ψ_2} is unchanged. The curves are fits to function $f(x) = Ce^{\xi x^2/2}$.

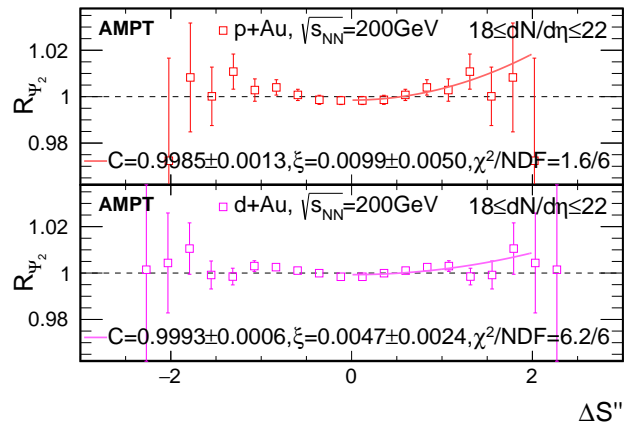


FIG. 2. R_{Ψ_2} distributions in $18 \leq dN/d\eta \leq 22$ from AMPT simulations for p+Au collisions (upper pad) and d+Au collisions (lower pad) at $\sqrt{s_{NN}} = 200$ GeV. Each dataset has 300 million MB events; 7.3 and 33.2 million analyzed p+Au and d+Au events in the $dN/d\eta$ range, respectively. The POI are required to have $0.35 \text{ GeV}/c < p_T < 2.0 \text{ GeV}/c$ and come from the p/d-going range $0.1 < \eta < 1.0$, whereas the particles used for EP reconstruction are required to have $0.2 \text{ GeV}/c < p_T < 2.0 \text{ GeV}/c$ and come from the Au-going range $-1.0 < \eta < -0.1$. The R_{Ψ_2} distributions are symmetrized. The R_{Ψ_2} from both p+Au and d+Au are slightly concave. The curves are fits to function $f(x) = Ce^{\xi x^2/2}$.

in Fig. 1 demonstrate that the R_{Ψ_2} and R_{Ψ_3} are not necessarily the same when only pure background is present. We speculate that the difference roots in the R_{Ψ_m} definitions: the “harmonic” multiplier $m/2$ in front of the azimuthal angle $\phi - \Psi_m$ (see Eq. 3) renders actually two distinctly different variables of R_{Ψ_2} and R_{Ψ_3} .

Moreover, as pointed out in Ref. [20], the R_{Ψ_3} variable is ill-defined because it breaks the natural azimuthal periodicity of 2π . The R_{Ψ_3} in blue circles in Fig. 1 uses the azimuthal range of $\phi \in [-\pi, \pi)$. If it is switched to $\phi \in [0, 2\pi)$ by adding 2π to those in the range $[-\pi, 0)$, with no change in physics, minus signs appear to the corresponding terms in Eq. 3, and the R_{Ψ_3} distribution changes completely to the magenta triangles in Fig. 1. The R_{Ψ_2} is of course unchanged by the choice of the ϕ range. Since R_{Ψ_3} is ill-defined [20], we will only focus on R_{Ψ_2} in the rest of this paper.

We note that a recent publication [30] appeared with similar AMPT results as those in the STAR work [21]. An examination of the statistical errors suggests [31] that those AMPT results in Ref. [30] are highly improbable to be real, calling into question the validity of those AMPT results. Moreover, concave R_{Ψ_m} distributions were observed by several other model studies for Au+Au collisions at $\sqrt{s_{NN}} = 200$ GeV. Those include hydrodynamic simulations [19] and toy model studies [20].

3.2. p+Au and d+Au collisions

For the small systems p+Au and d+Au collisions at $\sqrt{s_{NN}} = 200$ GeV, total 300 million MB AMPT events each are simulated. Since the centrality is not well-defined in those small systems, we cut on the reference multiplicity $18 \leq dN/d\eta \leq 22$ (the number of charged particles in the range $-0.5 < \eta < 0.5$), a range similar to the STAR data analysis [21]. These correspond to 7.3 and 33.2 million analyzed events for p+Au and d+Au collisions, respectively. As same as in Ref. [21], the event plane is reconstructed from the particles in the Au-going direction in the range of $-1.0 < \eta < -0.1$, and the POI’s are from the p/d-going direction in the range of $0.1 < \eta < 1.0$. The η gap between the EP particles and the POI’s suppresses short-range correlations.

Figure 2 shows the R_{Ψ_2} distributions in the small system collisions by AMPT. The distributions are slightly concave, and appear qualitatively different from the STAR data [21], where the R_{Ψ_2} curve in p+Au collisions is flat and that in d+Au collisions is flat or even convex. Since the CME signal is either absent or uncorrelated with the reconstructed EP in those small systems, the flat R_{Ψ_2} curves were important for the conclusion in Ref. [21] that the R_{Ψ_2} is sensitive to CME and relatively insensitive to backgrounds which do have strong effects on the $\Delta\gamma$ observable [10, 11]. Our AMPT results in p+Au and d+Au collisions suggest that this may not be the case.

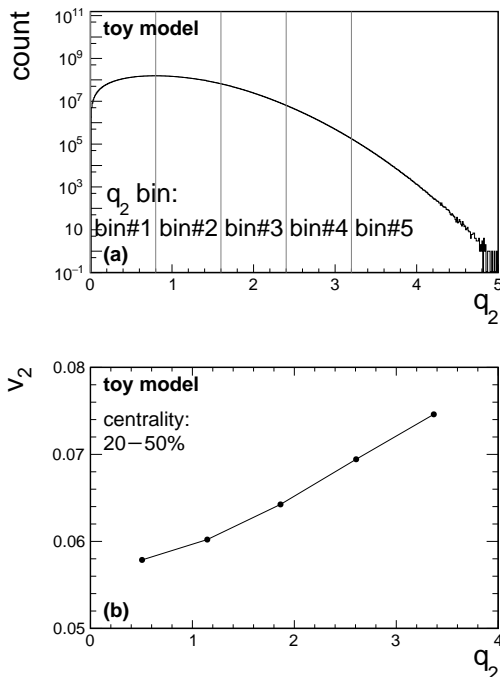


FIG. 3. (a) The q_2 distribution for 20–50% Au+Au collisions simulated by the toy model using STAR data as input parameters. This is used in ESE analysis where q_2 bins are divided by q_2 values of equal spacing (except the last bin). (b) The v_2 vs. q_2 of each ESE q_2 bin. Total 10.9 billion events are simulated for centrality 20–50%. The q_2 is calculated from particles in $|\eta| < 0.3$ with $0.2 \text{ GeV}/c < p_T < 2.0 \text{ GeV}/c$, whereas v_2 is calculated from particles in $|\eta| > 0.3$ with $0.2 \text{ GeV}/c < p_T < 2.0 \text{ GeV}/c$.

4. ESE STUDY IN A TOY MODEL

STAR performed an ESE analysis of their Au+Au data [21]. Each event is divided into three subevents: east ($-1 < \eta < -0.3$), middle ($-0.3 < \eta < 0.3$) and west ($0.3 < \eta < 1.0$) subevents. The middle subevent is used to calculate the q_2 quantity,

$$q_2 = \sqrt{\frac{\left(\sum_i^M \cos 2\phi_i\right)^2 + \left(\sum_i^M \sin 2\phi_i\right)^2}{M}}, \quad (15)$$

where M is the number of particles in the middle subevent. This quantity is related to the elliptical shape of the corresponding subevent in momentum space. The events are then divided according to the q_2 value, and are analyzed separately in each q_2 class. In each event, the east and west subevents are used to calculate the elliptic flow v_2 and the R_{Ψ_2} correlator by the subevent method (Eqs. 3–10). It was found that the v_2 increases with increasing q_2 but the R_{Ψ_2} width is independent of q_2 within uncertainties. This would imply that the width of R_{Ψ_2} is independent from the event-by-event v_2 in each q_2 class. This renders support to the claim in Ref. [21] that the

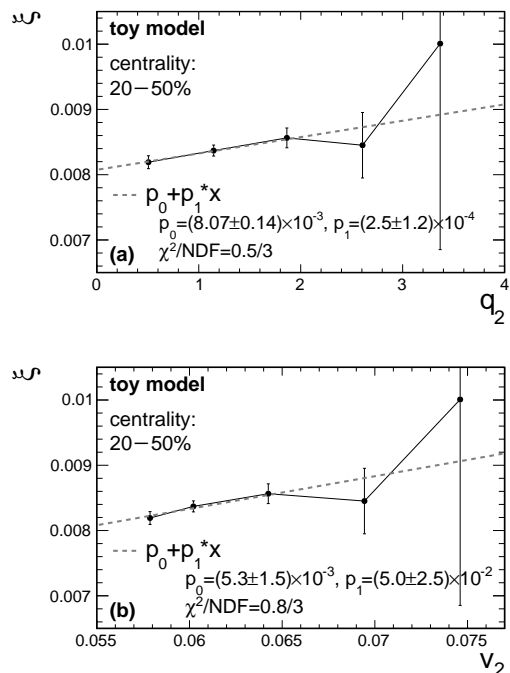


FIG. 4. (a) The ξ vs. q_2 of each ESE q_2 bin for centrality 20–50% Au+Au collisions simulated by the toy model using STAR data as input parameters. Total 10.9 billion events are simulated for centrality 20–50%. The POI are required to have $0.35 \text{ GeV}/c < p_T < 2.0 \text{ GeV}/c$ and $0.3 < \pm\eta < 1.0$, whereas particles for EP reconstruction are required to have $0.2 \text{ GeV}/c < p_T < 2.0 \text{ GeV}/c$ and $0.3 < \mp\eta < 1.0$. (b) The mapping of ξ as a function of v_2 in each ESE q_2 bin.

R_{Ψ_2} is relatively insensitive to the flow background.

However, our previous toy model study [20] shows that R_{Ψ_2} has dependence on event-wise v_2 . This seems to contradict the claim from the ESE study in Ref. [21]. To investigate this further, we carry out an ESE analysis using the toy model [20, 32]. The toy model is used instead of a physics model such as AMPT because the ESE analysis typically requires large statistics that is difficult to achieve by the latter. The toy model includes primordial pions and ρ meson decay daughters [20, 32]. The inputs to the toy model are taken from real data of Au+Au collisions at 200 GeV for each of the 10%-size centrality bins. These include the pion and ρ meson p_T distributions and $v_2(p_T)$ [32–42]. The p_T spectra measurements of the ρ mesons are limited to 40–80% centrality; the p_T spectra shapes are assumed to be centrality independent in our simulation. The $v_{2,\rho}(p_T)$ are parameterized according to the number of constituent quark (NCQ) scaling. Fluctuations are added for v_2 by a Gaussian distribution with a relative width of 40% from event to event. The ρ/π multiplicity ratio is approximately $n_\rho/n_\pi = 0.085$, assumed to be centrality independent, and their multiplicities are such that the total final multiplicity matches mid-rapidity data for each given centrality bin [32]. Particles are generated with $|\eta| < 1.5$ assuming multiplicity

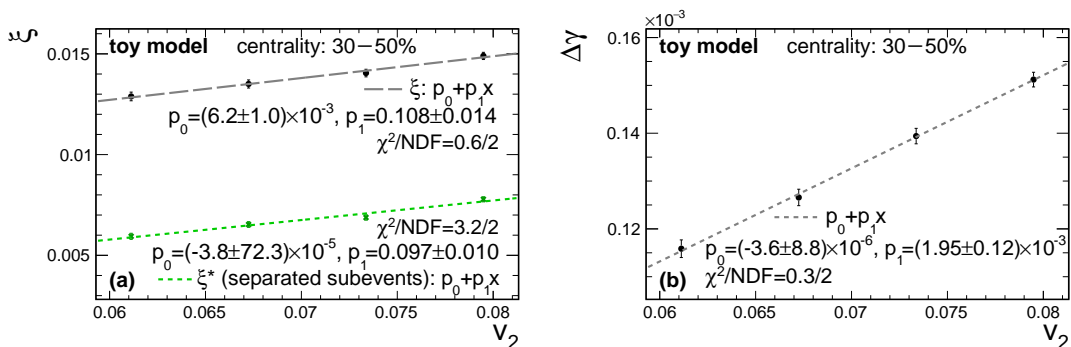


FIG. 5. The ξ and ξ^* (a) and $\Delta\gamma$ (b) as functions of the input v_2 from Au+Au collisions at $\sqrt{s_{NN}} = 200$ GeV with no CME signal. The leftmost data point uses the default v_2 distributions; other points use v_2 distributions that are scaled up accordingly. Each data point has total 2 billion toy model events in the 0–80% centrality range (or 0.73 billion events in the 30–50% centrality range). The POI are required to have $0.35 \text{ GeV}/c < p_T < 2.0 \text{ GeV}/c$ and $0.1 < \pm\eta < 1.0$, whereas particles for EP reconstruction are required to have $0.2 \text{ GeV}/c < p_T < 2.0 \text{ GeV}/c$ and $0.1 < \mp\eta < 1.0$. For each dataset, the ξ , ξ^* , $\Delta\gamma$, and v_2 are calculated from centrality range 30–50% (average multiplicity $dN/d\eta \approx 140$, average subevent POI multiplicity $N_{ch} \approx 64$). The dashed lines are two-parameter linear fits.

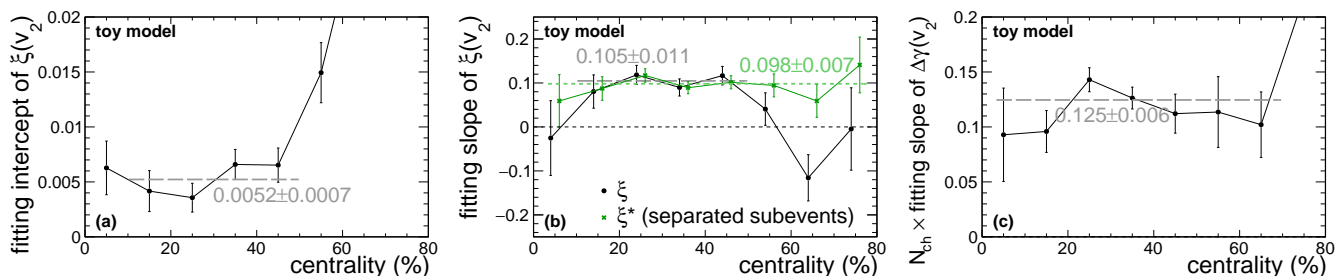


FIG. 6. The fit parameters from linear fits to $\xi(v_2)$, $\xi^*(v_2)$, and $\Delta\gamma(v_2)$ are plotted as functions of centrality. The ξ , ξ^* , $\Delta\gamma$ are similar to those in Fig. 5, but are calculated for each narrow centrality bin of 10% size. (a) The $\xi(v_2)$ intercept, which is roughly constant in the centrality range 10–50%. The $\xi^*(v_2)$ and $\Delta\gamma(v_2)$ intercepts are all consistent with zero. (b) The slopes of $\xi(v_2)$ and $\xi^*(v_2)$, which seem to be independent of centrality. (c) The $\Delta\gamma(v_2)$ slope multiplied by N_{ch} . The slope is inversely proportional to N_{ch} .

density is uniform in η . For a given centrality bin of 10% size, we take its mean multiplicity from data and use a corresponding Poisson distribution to sample the multiplicity of each event. In this ESE analysis, only middle centrality events are used; the average multiplicity is $dN/d\eta \approx 179$ in the range $-0.5 < \eta < 0.5$. In short, the default setting of this toy model mimics the Au+Au collisions at $\sqrt{s_{NN}} = 200$ GeV. Total 10.9 billion events are simulated for centrality 20–50%.

We followed the STAR analysis by dividing the $|\eta| < 1$ particles in the toy model into three (east, west, and middle) subevents. The q_2 distribution from the middle subevents is shown in Fig. 3. For the q_2 binning, equal q_2 size (except the last q_2 bin) is taken [21], which is indicated by the vertical lines in Fig. 3. The five bins are labeled as bin#1, bin#2, bin#3, bin#4, and bin#5, respectively, corresponding to the notations 0–20%, 20–40%, 40–60%, 60–80%, and 80–100% in Ref. [21]. We calculate the average q_2 values for each ESE q_2 bin of Fig. 3 (a). The elliptic flow of the east and west subevent

are obtained from the two-particle cumulant method,

$$v_2 = \sqrt{\langle \cos 2(\phi_{aE} - \phi_{bW}) \rangle}, \quad (16)$$

where a is a particle from east subevent and b from west subevent. Figure 3 (b) shows v_2 as a function of the q_2 . The v_2 is found to increase with q_2 , indicating some level of selectivity of v_2 by q_2 .

Figure 4 shows ξ as functions of q_2 and v_2 . The fits show that ξ increases with q_2 and v_2 , with the slope parameters deviating from zero by approximately 2 standard deviations, with the current 10.9 billion events simulated for 20–50% centrality. We can make two observations from our ESE study: (1) the ξ does depend on v_2 ; and (2) such ESE studies require humongous statistics in order to draw clear conclusions. The latter is probably the primary reason why STAR did not observe a q_2 dependence of ξ with their limited statistics of ~ 200 million events for 20–50% centrality Au+Au collisions [21]. With the large uncertainties in Ref. [21], it is premature to draw the conclusion “ R_{Ψ_2} is relatively insensitive to

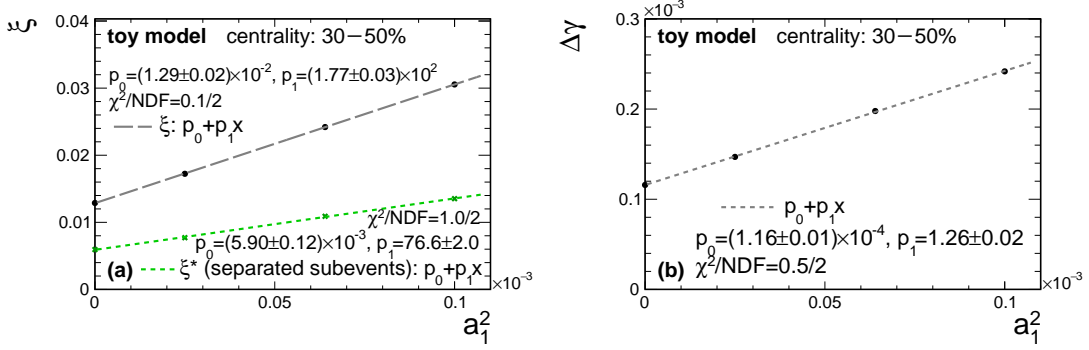


FIG. 7. The ξ and ξ^* (a) and $\Delta\gamma$ (b) as functions of the input CME signal (a_1^2) from the toy model simulations for Au+Au collisions at $\sqrt{s_{NN}} = 200$ GeV with default v_2 distribution. Each data point has total 2 billion toy model events in the 0–80% centrality range (or 0.73 billion events in the 30–50% centrality range). The POI are required to have $0.35 \text{ GeV}/c < p_T < 2.0 \text{ GeV}/c$ and $0.1 < \pm\eta < 1.0$, whereas particles for EP reconstruction are required to have $0.2 \text{ GeV}/c < p_T < 2.0 \text{ GeV}/c$ and $0.1 < \mp\eta < 1.0$. For each dataset, the ξ , ξ^* , $\Delta\gamma$, and v_2 are calculated from centrality range 30–50% (average multiplicity $dN/d\eta \approx 140$, average subevent POI multiplicity $N_{ch} \approx 64$). The dashed lines are two-parameter linear fits.

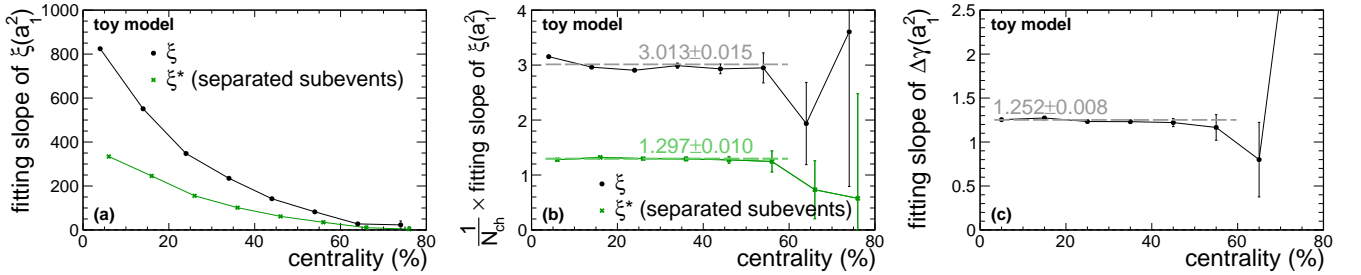


FIG. 8. The fit parameters from linear fits to $\xi(a_1^2)$, $\xi^*(a_1^2)$, and $\Delta\gamma(a_1^2)$ are plotted as functions of centrality. The ξ , ξ^* , $\Delta\gamma$ are similar to those in Fig. 7, but are calculated for each narrow centrality bin of 10% size. (a) The $\xi(a_1^2)$ and $\xi^*(a_1^2)$ slopes, which are decreasing with increasing centrality percentile (or decreasing centrality). (b) The $\xi(a_1^2)$ and $\xi^*(a_1^2)$ slopes divided by N_{ch} . The slopes are proportional to N_{ch} . (c) The $\Delta\gamma(a_1^2)$ slope, which seems to be independent from centrality.

v_2 ” [21].

5. TOY MODEL STUDY TO DECIPHER R_{Ψ_2}

We use the toy model in Sec. 4 to further study the sensitivity of R_{Ψ_2} to background v_2 and signal a_1 in Au+Au and isobar collisions. We simulate all centrality bins measured in data, namely 0–80%. To investigate the middle central collisions in greater details, each 10%-size bin in 20–50% (20–60%) centrality range has twice as many events as other 10%-size centrality bins in Au+Au (isobar) collisions.

5.1. Sensitivity to v_2 background

The toy model datasets are simulated with various input $v_2(p_T)$, including the default v_2 and variations with 10%, 20%, and 30% increase from the default v_2 . For each dataset of a given input v_2 , the ξ and v_2 of final-state particles are calculated. Figure 5 (a) maps those

two variables for the 30–50% centrality and a linear dependence is observed between them. Previous toy model study also observed a R_{Ψ_2} dependence on v_2 (and transverse momentum p_T) [20].

Similarly, $\Delta\gamma$ is also calculated from those datasets with the same cuts, and is shown in Fig. 5 (b). A linear dependence on v_2 is also observed, as one expects for the background behavior in $\Delta\gamma$ as discussed in Sec. 2.2 (cf. Eq. 14). First-order polynomial fit yields an intercept consistent with zero for $\Delta\gamma(v_2)$. This is expected because the $\Delta\gamma$ will go to zero where there is no elliptic flow.

However, first-order polynomial fit to $\xi(v_2)$ yields a nonzero intercept. This is shown in Fig. 5 (a). The fit parameters are consistent with those from the ESE study shown in Fig. 4 (b), modulo the large errors for the latter. The nonzero intercept arises because of the additional correlation between POI and EP brought by averaging the two subevents in Eq. 4,

$$\begin{aligned} \text{Var}[\Delta S] &= \langle \Delta S^2 \rangle \\ &= \frac{1}{4} \langle (\Delta S^E)^2 \rangle + \frac{1}{4} \langle (\Delta S^W)^2 \rangle + \frac{1}{2} \langle \Delta S^E \Delta S^W \rangle. \end{aligned} \quad (17)$$

This auto-correlation comes about because the POI for ΔS^E are used for EP reconstruction for ΔS^W , and vice versa. To circumvent this, we count the two subevents separately instead of combining them. The squared inverse width of $R_{\Psi_2}(\Delta S'')$ obtained from this method, is referred to as ξ^* . The $\xi^*(v_2)$ is shown in Fig. 5 (a). A linear dependence is observed, with an intercept consistent with zero. In fact, the difference between ξ and ξ^* at any given setting (i.e. not just the intercept as we noted above) is caused by the auto-correlation. This will be discussed further in Appendix A.2 and A.3

We repeat the fit for each narrow centrality bin. In Fig. 6 (a), the fit intercept parameter is shown as a function of centrality for $\xi(v_2)$, which seems roughly a constant in the centrality range 10–50%. In Fig. 6 (b), the fit slope parameter is shown as functions of centrality for $\xi(v_2)$, $\xi^*(v_2)$. The $\xi(v_2)$ ($\xi^*(v_2)$) slope is roughly constant in the centrality range 10–50% with a value approximately 0.105 (0.098). See Appendix B.1 for an analytical derivation.

Figure 6 (c) shows the slope of $\Delta\gamma(v_2)$ multiplied by N_{ch} , where N_{ch} is average POI multiplicity of each subevent in $-1.0 < \eta < -0.1$ (or $0.1 < \eta < 1.0$) with $p_T > 0.35$ GeV/c. It is found that the slope parameter of $\Delta\gamma(v_2)$ is inversely proportional to multiplicity, with a dependence approximately $0.125/N_{ch}$. This is consistent with previous findings that the $\Delta\gamma$ is diluted by multiplicity, as discussed in Sec. 2.2 (cf. 14). See further details in Appendix C.

To summarize, the ξ , ξ^* , and $\Delta\gamma$ can be parameterized, empirically for the given toy model simulation in this study without CME signal input, as

$$\xi_{\text{bkgd}} \approx (0.105 \pm 0.011)v_2 + (0.0052 \pm 0.0007), \quad (18a)$$

$$\xi_{\text{bkgd}}^* \approx (0.098 \pm 0.007)v_2, \quad (18b)$$

$$\Delta\gamma_{\text{bkgd}} \approx (0.125 \pm 0.006)v_2/N_{ch}. \quad (18c)$$

5.2. Responses to CME signal

To study the sensitivity to CME signal, we input an a_1 parameter into particle distribution in the toy model, keeping the default setting for the v_2 background. We set a_1 to 0, 0.005, 0.008, and 0.010. For each case, we generate 2 billion events over 0–80% centrality, where 0.73 billion events are in 30–50% centrality.

The ξ , ξ^* , and $\Delta\gamma$ are calculated from centrality range 30–50%. Figure 7 (a) and (b) show the ξ , ξ^* and $\Delta\gamma$ as functions of a_1^2 . Linear dependence on a_1^2 is observed for all observables. Linear fits are superimposed in Fig. 7 (a,b). All show nonzero intercepts, corresponding to the backgrounds caused by the nonzero v_2 in the underlying events.

The similar procedure above is then repeated for each narrow centrality bin. Figure 8 (a) shows the fit slope parameters as functions of centrality for $\xi(a_1^2)$, $\xi^*(a_1^2)$. The $\xi(a_1^2)$ slope is found to decrease with centrality percentile (or increase with centrality); it is found to be pro-

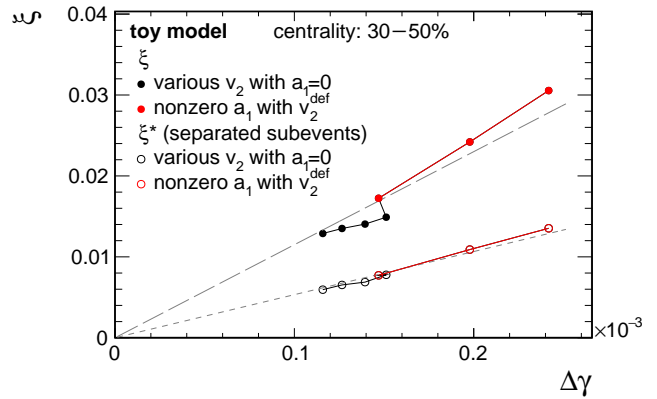


FIG. 9. The ξ (ξ^*) and $\Delta\gamma$ are mapped for each toy model simulation for Au+Au collisions at $\sqrt{s_{NN}} = 200$ GeV in Fig. 5 (various input v_2 distributions with no CME signal, first four data points) and Fig. 7 (various input a_1 values with default v_2 distribution, last three data points). The lines are one-parameter linear fits to the data points, mainly to guide the eye.

portional to multiplicity (Fig. 8 (b)). See Appendix B.2 for an analytical derivation.

Figure 8 (c) shows the fit slope parameters as a function of centrality for $\Delta\gamma(a_1^2)$. The $\Delta\gamma(a_1^2)$ slope parameter is found to be independent of the centrality, and intercept is always consistent with zero. Ideally one expect $\Delta\gamma$ to vary as $2a_1^2$ (Eq. 13). The slope parameter from our toy model is found to be ~ 1.252 , smaller than 2; this is because the CME signal a_1 is applied only to primordial pions, not to the secondary pions from resonance decays. See further details in Appendix C. If parameter a_1 characterizes the coefficient in Eq. 1 which includes all final-state particles, then we would have $\Delta\gamma = 2a_1^2$.

To summarize, the CME signal dependence of the ξ , ξ^* , and $\Delta\gamma$ can be parameterized, empirically for the given toy model simulation in this study, as

$$\xi_{\text{CME}} \approx (3.013 \pm 0.015)a_1^2 N_{ch}, \quad (19a)$$

$$\xi_{\text{CME}}^* \approx (1.297 \pm 0.010)a_1^2 N_{ch}, \quad (19b)$$

$$\Delta\gamma_{\text{CME}} \approx (1.252 \pm 0.008)a_1^2. \quad (19c)$$

5.3. Relative merits of R_{Ψ_2} and $\Delta\gamma$

To summarize the findings in Sec. 5.1 and 5.2, we can parameterize ξ , ξ^* , and $\Delta\gamma$ in terms of the v_2 background and the CME signal, in our toy model simulation

of Au+Au 10–50% centrality, by:

$$\xi/N_{ch} \approx (0.105 \pm 0.011)v_2/N_{ch} + (3.013 \pm 0.015)a_1^2 + (0.0052 \pm 0.0007)/N_{ch}, \quad (20a)$$

$$\xi^*/N_{ch} \approx (0.098 \pm 0.007)v_2/N_{ch} + (1.297 \pm 0.010)a_1^2, \quad (20b)$$

$$\Delta\gamma \approx (0.125 \pm 0.006)v_2/N_{ch} + (1.252 \pm 0.008)a_1^2. \quad (20c)$$

It is worthwhile to note that ξ/N_{ch} , and specially ξ^*/N_{ch} , is rather similar to $\Delta\gamma$. This may not be surprising as the ξ is related to the combination of the ΔS and ΔS^\perp variances, roughly $\langle \cos(\phi_a - \Psi_{RP}) \cos(\phi_b - \Psi_{RP}) - \sin(\phi_a - \Psi_{RP}) \sin(\phi_b - \Psi_{RP}) \rangle$, which is the $\Delta\gamma$ [43]. In Appendix B, we provide an analytical derivation of ξ^* without considering correlations arising from p_T dependence of v_2 and decay kinematics, etc. Our toy model results above and the analytical estimates are qualitatively consistent. Our analytical results are also qualitatively in line with findings by others [44].

We may estimate the signal/background ratio (S/B) of the two observables from Eq. 20, within our toy model simulation, as

$$\xi: \quad S/B \approx \frac{(28.7 \pm 3.0)a_1^2 N_{ch}}{v_2 + (0.050 \pm 0.008)}, \quad (21a)$$

$$\xi^*: \quad S/B \approx (13.2 \pm 1.0)a_1^2 N_{ch}/v_2 \quad (21b)$$

$$\Delta\gamma: \quad S/B \approx (10.0 \pm 0.5)a_1^2 N_{ch}/v_2. \quad (21c)$$

Thus, in terms of the S/B value, ξ^* is more (less) sensitive to signal (background) than $\Delta\gamma$ with this toy model in this centrality range.

We can map the observables ξ vs. $\Delta\gamma$ and ξ^* vs. $\Delta\gamma$ against each other using the data in Sec. 5.1 and 5.2, as shown in Fig. 9. There is a monotonic, one-to-one correspondence between ξ^* and $\Delta\gamma$, indicating that they are essentially equivalent in searching for the CME. A recent AMPT simulation study also shows that the R_{Ψ_2} and $\Delta\gamma$ observables are essentially equivalent [45]. For ξ and $\Delta\gamma$, there are two groups of data points with different slopes, one from background variation and the other from signal variation. This is likely caused by the auto-correlations arising from averaging ΔS between subevents discussed in Sec. 5.1 and Appendix A. Our toy model study only includes ρ decays, while the real collisions have also other resonances whose decay kinematics are different from the ρ 's. This can render possible quantitative changes in the relative merits of $\Delta\gamma$ and ξ , ξ^* .

It is worthwhile to note, however, that the $\Delta\gamma$ observable is relatively straightforward to interpret whereas the R_{Ψ_m} observable is complex. The $\Delta\gamma$ variable is computed per particle pair and the ξ (ξ^*) variable is computed per event. The former offers a wider versatility in ways to isolate the CME signal from backgrounds, for example, a differential study in pair invariant mass [10, 46–48]. Although ξ (ξ^*) may have a slightly larger S/B value than $\Delta\gamma$ according to our toy model study, both are

strongly affected by physics backgrounds which dominate over the CME. Both observables have to seek innovative ways to isolate the CME signal and physics backgrounds. One of the promising ways is to leverage on the different harmonic planes in the same collision event for $\Delta\gamma$ measurements [49–51]. It would be interesting to study the benefit of applying such a method to ξ (ξ^*).

5.4. Isobar background expectations

Recently, $^{96}_{44}\text{Ru}+^{96}_{44}\text{Ru}$, and $^{96}_{40}\text{Zr}+^{96}_{40}\text{Zr}$ collisions have been conducted at RHIC to potentially resolve the background issue in the search for CME. Those two species are isobars of each other, with the same number of nucleons ($A = 96$) but different number of protons ($Z = 44, 40$). The backgrounds are expected to be similar in those two collision systems due to the same nucleon number. The CME signals should be quite different due to the different magnetic fields created by the spectator protons whose numbers are different in those isobars. There may be complications to these simple expectations when considering modern nuclear structure calculations [50, 52].

Both the R_{Ψ_m} and the inclusive $\Delta\gamma$ correlators are employed to search for the CME using the isobar data [53]. To examine the relative merits of the two observables in searching for the CME, we simulate Ru+Ru and Zr+Zr collisions using the toy model. The multiplicity is scaled from Au+Au by the number of participant nucleons. We use the following inputs for the Zr+Zr and Ru+Ru collision systems, respectively.

- Zr+Zr: default $v_{2,\pi}(p_T)$ and $v_{2,\rho}(p_T)$ (as same as those used in the default Au+Au toy model simulation), and the CME signal $a_1 = 0.50\%$;
- Ru+Ru: 2% larger $v_{2,\pi}$ and $v_{2,\rho}$, and a 10% larger CME signal than in Zr+Zr. The 2% larger v_2 is guided by the expected v_2 difference from modern nuclear structure calculations [50, 52]. The 10% larger CME signal comes from the 10% more protons in the Ru than Zr nucleus.

Figure 10 shows the Ru+Ru over Zr+Zr ratio of ξ in the two isobar systems, along with that of $\Delta\gamma$. The centrality dependence of the ratios can be understood by Eq. 20. For $\Delta\gamma$, the ratio is

$$\begin{aligned} & \frac{\Delta\gamma(\text{Ru+Ru})}{\Delta\gamma(\text{Zr+Zr})} \\ &= \frac{1.252a_1^2 \times 1.1^2 + 0.125v_2/N_{ch} \times 1.02}{1.252a_1^2 + 0.125v_2/N_{ch}} \\ &= 1.21 - \frac{0.19 \times 0.125v_2}{1.252a_1^2 N_{ch} + 0.125v_2} \\ &= 1.02 + \frac{0.19 \times 1.252a_1^2 N_{ch}}{1.252a_1^2 N_{ch} + 0.125v_2}, \end{aligned} \quad (22)$$

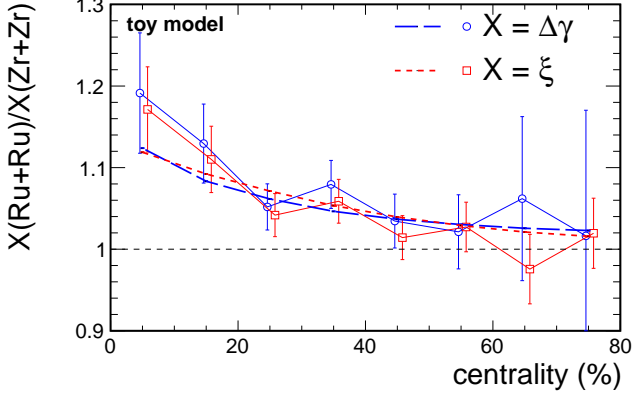


FIG. 10. The ratio between the observable X in the two collision systems as functions of the centrality, where X is ξ or $\Delta\gamma$. For Zr+Zr, the default v_2^{def} and CME signal $a_1 = 0.005$ are input, whereas for Ru+Ru, the $1.02v_2^{\text{def}}$ and $a_1 = 0.0055$ are input. Each dataset has 3 billion toy model events in the 0–80% centrality range, where 2 billion events are in 20–60% centrality range. The POI are required to have $0.35 \text{ GeV}/c < p_T < 2.0 \text{ GeV}/c$ and $0.1 < \pm\eta < 1.0$, whereas particles for EP reconstruction are required to have $0.2 \text{ GeV}/c < p_T < 2.0 \text{ GeV}/c$ and $0.1 < \mp\eta < 1.0$. The curves are given by Eqs. 22 and 24.

and the double ratio is

$$\begin{aligned}
 & \frac{\Delta\gamma(\text{Ru+Ru})/v_2(\text{Ru+Ru})}{\Delta\gamma(\text{Zr+Zr})/v_2(\text{Zr+Zr})} \\
 &= \frac{\Delta\gamma(\text{Ru+Ru})}{\Delta\gamma(\text{Zr+Zr})} \times \frac{1}{1.02} \\
 &= 1.186 - \frac{0.186 \times 0.125v_2}{1.252a_1^2 N_{ch} + 0.125v_2} \\
 &= 1 + \frac{0.186 \times 1.252a_1^2 N_{ch}}{1.252a_1^2 N_{ch} + 0.125v_2}.
 \end{aligned} \tag{23}$$

For ξ , the ratio is

$$\begin{aligned}
 & \frac{\xi(\text{Ru+Ru})}{\xi(\text{Zr+Zr})} \\
 &= \frac{3.013a_1^2 \times 1.1^2 + 0.105v_2/N_{ch} \times 1.02 + 0.0052/N_{ch}}{3.013a_1^2 + 0.105v_2/N_{ch} + 0.0052/N_{ch}} \\
 &= 1.21 - \frac{0.19 \times 0.105v_2 + 0.21 \times 0.0052}{3.013a_1^2 N_{ch} + 0.105v_2 + 0.0052} \\
 &= 1.02 + \frac{0.19 \times 3.013a_1^2 N_{ch} - 0.02 \times 0.0052}{3.013a_1^2 N_{ch} + 0.105v_2 + 0.0052}.
 \end{aligned} \tag{24}$$

The last two lines of Eqs. 22, 23, and 24 are different ways to express the ratios to illustrate the limits. In the limit of high multiplicity $N_{ch} \rightarrow \infty$ (centrality $\rightarrow 0\%$), the ratios go to 1.21, and the double ratio goes to 1.186. In the limit of low multiplicity $N_{ch} \rightarrow 0$ (centrality $\rightarrow 80\%$), the ratios go to 1.02 ($\Delta\gamma$) or ~ 1.01 (ξ), and the

double ratio goes to 1. We superimpose in Fig. 10 the parameterizations of Eqs. 22 and 24. Since the trends and statistic errors are similar for ξ and the inclusive $\Delta\gamma$, as evident from Fig. 10, the two observables would serve the same functionality in searching for the CME in isobar collisions; neither seems superior to the other. The conclusion is the same if ξ^* is used instead of ξ .

It is worthwhile to note that our toy model simulation is useful and informative to reveal the relative merits of the R_{Ψ_2} and $\Delta\gamma$ observables within the same simulated data. One, however, should not take the magnitudes and error bars of the points in Fig. 10 to infer those of the real isobar data. Even though we simulated the similar number of events as in data, the physics included in our toy model is overly simplified (e.g., only ρ resonance is included) and the CME signal is, of course, an arbitrary input.

6. SUMMARY

We have studied the R_{Ψ_m} correlators using the AMPT model, which does not include any CME signal. With Au+Au collisions at $\sqrt{s_{NN}} = 200 \text{ GeV}$ simulated by AMPT, the R_{Ψ_2} distribution is concave. The R_{Ψ_3} distribution, with the choice of the azimuthal angle range of $\phi \in [-\pi, \pi)$, is concave and differs from that of R_{Ψ_2} , but with the choice $\phi \in [0, 2\pi)$, it is approximately flat indicating the illness of the R_{Ψ_3} definition [20]. The same AMPT model is also used to simulate small-system p+Au and d+Au collisions at $\sqrt{s_{NN}} = 200 \text{ GeV}$. The R_{Ψ_2} distributions are found to be slightly concave in those small-system collisions.

We have used a toy model to generate primordial and resonance decay pions, according to kinematic distributions and elliptic flow measured in 200 GeV Au+Au collision data. It is found that the R_{Ψ_m} distribution squared inverse width (ξ^*) is proportional to v_2 . We verified the approximate linearity with algebraic derivation. In addition, we find that the usual implementation of R_{Ψ_2} by averaging subevents introduces an auto-correlation that causes an intercept in the $\xi(v_2)$ linear dependence. We have also input CME signal into the toy model via the a_1 parameter. It is found that the ξ and ξ^* increase linearly with $N_{ch}a_1^2$, where N_{ch} is the multiplicity of the particles of interests. We have also calculated the $\Delta\gamma$ correlator and found the expected linear dependence on v_2/N_{ch} and on a_1^2 . Except the multiplicative factor of N_{ch} , the dependences on v_2 and a_1^2 are rather similar between ξ^* and $\Delta\gamma$, and also between ξ and $\Delta\gamma$.

The toy model simulation, with only v_2 background, is also used for an event shape engineering study. It is found that the ξ does depend on the event-by-event q_2 and v_2 at 2 sigma significance with 10.9 billion events corresponding to 20–50% centrality Au+Au collisions.

The toy model is also used to simulate the isobar systems at $\sqrt{s_{NN}} = 200 \text{ GeV}$. With the anticipated 10% CME signal (a_1) and 2% flow background (v_2) differ-

ences, the ξ and the inclusive $\Delta\gamma$ relative strengths between the isobar collision systems have rather similar trend on centrality, with similar magnitudes and statistical uncertainties. It appears that the two observables are essentially the same; neither observable has advantage over the other.

It has been argued [21] that (i) the R_{Ψ_2} and R_{Ψ_3} distributions were identical for pure background scenarios, (ii) the small-system collisions yield flat R_{Ψ_2} distributions, and (iii) the R_{Ψ_2} distribution does not depend on q_2 with event shape engineering where variation in v_2 is observed. These corroborative features led to the conclusion that the concave R_{Ψ_2} distribution observed in Au+Au collisions, more strongly concave than the R_{Ψ_3} distribution, is inconsistent with known backgrounds and thus may suggest the presence of the CME signal [21]. Our studies indicate that none of the three features seems to uphold, and there appears to be no qualitative difference between the R_{Ψ_2} observable and the inclusive $\Delta\gamma$ correlator.

ACKNOWLEDGMENTS

This work is supported in part by the U.S. Department of Energy Grant No. DE-SC0012910 and the National Natural Science Foundation of China Grant Nos. 11905059, 12035006, 12047568, 12075085.

Appendix A: EP resolution corrections

In this appendix, we first derive the analytical form of the EP resolution correction factor (Eq. 7) for the squared inverse width of the R_{Ψ_m} correlator, ξ^* . We then discuss the empirical correction factor used by STAR [21]. Finally we investigate the effect of auto-correlations on ξ .

1. EP resolution correction for ξ^*

Ideally, one likes to use the RP Ψ_{RP} in Eq. 3 instead of subevent EP Ψ_m . In this section, we derive the correction factor on ΔS to take into account the inaccuracy of the reconstructed EP in representing the RP. To lighten notations, we do not explicitly specify the subevent by the superscript E/W , but rather implicitly refer to a given subevent for the ΔS_m and Ψ_m quantities.

The terms in ΔS_m can be written, taking one representative term as an example, into

$$\begin{aligned} & \sin\left(\frac{m}{2}(\phi^+ - \Psi_m)\right) \\ &= \sin\left(\frac{m}{2}(\phi^+ - \Psi_{\text{RP}})\right) \cos\left(\frac{m}{2}(\Psi_m - \Psi_{\text{RP}})\right) - \\ & \cos\left(\frac{m}{2}(\phi^+ - \Psi_{\text{RP}})\right) \sin\left(\frac{m}{2}(\Psi_m - \Psi_{\text{RP}})\right). \end{aligned} \quad (\text{A1})$$

Thus, the relationship between the ΔS_m variables w.r.t. Ψ_{RP} and Ψ_m are

$$\begin{aligned} \Delta S_m(\Psi_m) &= \Delta S_m(\Psi_{\text{RP}}) \cos\left(\frac{m}{2}(\Psi_m - \Psi_{\text{RP}})\right) - \\ & \Delta S_m^\perp(\Psi_{\text{RP}}) \sin\left(\frac{m}{2}(\Psi_m - \Psi_{\text{RP}})\right), \\ \Delta S_m^\perp(\Psi_m) &= \Delta S_m^\perp(\Psi_{\text{RP}}) \cos\left(\frac{m}{2}(\Psi_m - \Psi_{\text{RP}})\right) + \\ & \Delta S_m(\Psi_{\text{RP}}) \sin\left(\frac{m}{2}(\Psi_m - \Psi_{\text{RP}})\right). \end{aligned} \quad (\text{A2})$$

The relationship among the variances (corresponding to the squared widths of the ΔS distributions) are then

$$\begin{aligned} \sigma^2[\Delta S_m(\Psi_m)] &= \sigma^2[\Delta S_m(\Psi_{\text{RP}})] \frac{1+r_m}{2} + \\ & \sigma^2[\Delta S_m^\perp(\Psi_{\text{RP}})] \frac{1-r_m}{2}, \\ \sigma^2[\Delta S_m^\perp(\Psi_m)] &= \sigma^2[\Delta S_m^\perp(\Psi_{\text{RP}})] \frac{1+r_m}{2} + \\ & \sigma^2[\Delta S_m(\Psi_{\text{RP}})] \frac{1-r_m}{2}, \end{aligned} \quad (\text{A3})$$

where r_m is the resolution of the subevent EP (Eq. 8). For convenience, we denote the variances with respect to the RP by

$$\begin{aligned} \sigma_\uparrow &= \sigma[\Delta S_m(\Psi_{\text{RP}})], & \sigma_{\perp\uparrow} &= \sigma[\Delta S_m^\perp(\Psi_{\text{RP}})], \\ \sigma_\downarrow &= \sigma[\Delta S_{m,\text{sh}}(\Psi_{\text{RP}})], & \sigma_{\perp\downarrow} &= \sigma[\Delta S_{m,\text{sh}}^\perp(\Psi_{\text{RP}})]. \end{aligned} \quad (\text{A4})$$

Then Eq. A3 becomes

$$\begin{aligned} \sigma^2[\Delta S_m(\Psi_m)] &= \frac{\sigma_\uparrow^2 + \sigma_{\perp\uparrow}^2}{2} + \frac{\sigma_\uparrow^2 - \sigma_{\perp\uparrow}^2}{2} r_m, \\ \sigma^2[\Delta S_m^\perp(\Psi_m)] &= \frac{\sigma_\uparrow^2 + \sigma_{\perp\uparrow}^2}{2} - \frac{\sigma_\uparrow^2 - \sigma_{\perp\uparrow}^2}{2} r_m. \end{aligned} \quad (\text{A5})$$

For convenience of presentation, we write in the following the distributions in ΔS_m , $\Delta S_{m,\text{sh}}$, ΔS_m^\perp , and $\Delta S_{m,\text{sh}}^\perp$ all as Gaussians, with vanishing means, and variances σ_m , $\sigma_{m,\text{sh}}$, σ_m^\perp , and $\sigma_{m,\text{sh}}^\perp$. However, our end conclusion is general, independent of whether those distributions are Gaussians or not. Take the ΔS_m distribution as

$$\frac{dN_{\text{event}}}{N_{\text{event}}} = \frac{1}{\sqrt{2\pi}\sigma_m} e^{-\frac{\Delta S_m^2}{2\sigma_m^2}} d(\Delta S_m). \quad (\text{A6})$$

The scaled $\Delta S''$ distribution is

$$\frac{dN_{\text{event}}}{N_{\text{event}}} = \frac{\sigma_{m,\text{sh}}}{\delta_{r_m} \sqrt{2\pi}\sigma_m} e^{-\frac{\Delta S''^2}{2\delta_{r_m}^2} \frac{\sigma_{m,\text{sh}}^2}{\sigma_m^2}} d(\Delta S''_m). \quad (\text{A7})$$

The shape of the scaled C_{Ψ_m} distribution is then

$$C_{\Psi_m}(\Delta S''_m) = \frac{\sigma_{m,\text{sh}}}{\sigma_m} e^{-\frac{\Delta S''^2}{2\delta_{r_m}^2} \left(\frac{\sigma_{m,\text{sh}}^2}{\sigma_m^2} - 1\right)}. \quad (\text{A8})$$

Similarly, we get

$$C_{\Psi_m}^{\perp}(\Delta S''_m) = \frac{\sigma_{m,\text{sh}}^{\perp}}{\sigma_m^{\perp}} e^{-\frac{\Delta S''_m}{2\delta_{r_m}^2} \left(\frac{\sigma_{m,\text{sh}}^{\perp 2}}{\sigma_m^{\perp 2}} - 1 \right)}. \quad (\text{A9})$$

Finally the shape of the scaled R_{Ψ_m} correlator can be written as

$$\begin{aligned} R_{\Psi_m}(\Delta S''_m) &= \frac{C_{\Psi_m}(\Delta S''_m)}{C_{\Psi_m}^{\perp}(\Delta S''_m)} \\ &= \frac{\sigma_{m,\text{sh}} \sigma_m^{\perp}}{\sigma_{m,\text{sh}}^{\perp} \sigma_m} e^{-\frac{\Delta S''_m}{2\delta_{r_m}^2} \left(\frac{\sigma_{m,\text{sh}}^2}{\sigma_m^2} - \frac{\sigma_{m,\text{sh}}^{\perp 2}}{\sigma_m^{\perp 2}} \right)} \end{aligned} \quad (\text{A10})$$

The observable ξ^* is therefore defined as

$$\xi^* = -\frac{1}{\delta_{r_m}^2} \left(\frac{\sigma_{m,\text{sh}}^2}{\sigma_m^2} - \frac{\sigma_{m,\text{sh}}^{\perp 2}}{\sigma_m^{\perp 2}} \right), \quad (\text{A11})$$

so the effective width of $R_{\Psi_2}(\Delta S'')$ is $\sigma = 1/\sqrt{|\xi^*|}$. The positive (negative) ξ^* indicates concave (convex) shape of R_{Ψ_2} , and zero ξ^* indicates a flat distribution.

The measured quantity is of course

$$\xi_0^* \equiv - \left(\frac{\sigma_{m,\text{sh}}^2}{\sigma_m^2} - \frac{\sigma_{m,\text{sh}}^{\perp 2}}{\sigma_m^{\perp 2}} \right). \quad (\text{A12})$$

Plugging Eq. A5 into Eq. A12, we have

$$\begin{aligned} \xi_0^* &= \frac{\sigma_{\perp\downarrow}^2(1+r_m) + \sigma_{\downarrow}^2(1-r_m)}{\sigma_{\perp\uparrow}^2(1+r_m) + \sigma_{\uparrow}^2(1-r_m)} - \frac{\sigma_{\downarrow}^2(1+r_m) + \sigma_{\perp\downarrow}^2(1-r_m)}{\sigma_{\uparrow}^2(1+r_m) + \sigma_{\perp\uparrow}^2(1-r_m)} \\ &= \frac{\sigma_{\uparrow}^2 \sigma_{\perp\downarrow}^2 - \sigma_{\downarrow}^2 \sigma_{\perp\uparrow}^2}{(\sigma_{\uparrow}^2 + \sigma_{\perp\uparrow}^2)^2 - (\sigma_{\uparrow}^2 - \sigma_{\perp\uparrow}^2)^2 r_m^2} \times 4r_m \\ &\approx \frac{\sigma_{\uparrow}^2 \sigma_{\perp\downarrow}^2 - \sigma_{\downarrow}^2 \sigma_{\perp\uparrow}^2}{(\sigma_{\uparrow}^2 + \sigma_{\perp\uparrow}^2)^2} \times 4r_m \approx - \left(\frac{\sigma_{\downarrow}^2}{\sigma_{\uparrow}^2} - \frac{\sigma_{\perp\downarrow}^2}{\sigma_{\perp\uparrow}^2} \right) r_m, \end{aligned} \quad (\text{A13})$$

where the approximations use $(\sigma_{\uparrow}^2 + \sigma_{\perp\uparrow}^2)^2 \gg (\sigma_{\uparrow}^2 - \sigma_{\perp\uparrow}^2)^2$. This measured quantity is $\xi_0^* = \delta_{r_m}^2 \xi^*$ where δ_{r_m} is the correction factor for the resolution effect. This correction factor must be equal to unity when r_m is unity, so we have

$$\delta_{r_m} = \sqrt{r_m}. \quad (\text{A14})$$

To check Eqs. A13 and A14 numerically, a resolution scan is conducted using our toy model by randomly throwing away particles since the EP resolution is approximately proportional to the square-root of the used multiplicity. Specifically, particles for EP reconstruction are randomly kept by various probabilities (100%, 90%, ..., 10%, and 9%, 8%, ..., 1%), while the POI are intact. For each case, we use the measured widths $(\sigma_2, \sigma_{2,\text{sh}}, \sigma_2^{\perp}, \sigma_{2,\text{sh}}^{\perp})$ to calculate the quantity ξ_0^* by the r.h.s. of Eq. A12. To get the true ξ^* , we replace EP by RP since the latter is the true plane in the toy model

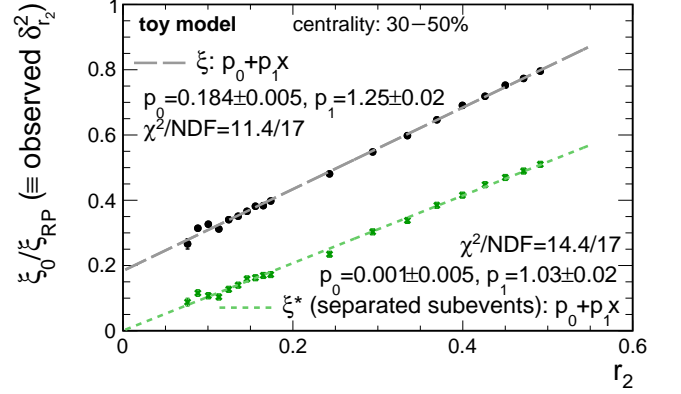


FIG. 11. The $\xi_0^*/\xi_{\text{RP}}^*$ and ξ_0/ξ_{RP} as functions of the EP resolution r_2 of subevents in Au+Au collisions at $\sqrt{s_{NN}} = 200$ GeV (no input CME signal). Total 4 billion toy model events in the 0–80% centrality range are used (or 1.46 billion events in the 30–50% centrality range). The POI are required to have $0.35 \text{ GeV}/c < p_T < 2.0 \text{ GeV}/c$ and $0.1 < \pm\eta < 1.0$, whereas particles for EP reconstruction are required to have $0.2 \text{ GeV}/c < p_T < 2.0 \text{ GeV}/c$ and $0.1 < \mp\eta < 1.0$. To scan the resolution, particles for EP reconstruction are randomly kept by various probabilities (100%, 90%, ..., 10%, and 9%, 8%, ..., 1%), while the POI are intact.

(fixed at $\Psi_{\text{RP}} = 0$). The ratio of the two, $\xi_0^*/\xi_{\text{RP}}^*$, is the square of the correction factor, $\delta_{r_2}^2$. Figure 11 shows the $\xi_0^*/\xi_{\text{RP}}^*$ as a function of the EP resolution r_2 of subevents in Au+Au collisions at $\sqrt{s_{NN}} = 200$ GeV (no input CME signal). The $\xi_0^*/\xi_{\text{RP}}^*$ has linear dependence on r_2 , and the first polynomial fit gives an intercept consistent with zero and a slope consistent with one, as predicted by Eq. A13.

2. The empirical EP resolution correction by STAR

In the derivation in Appendix A.1, we have treated the subevent $\Delta S^{E/W}$ separately. If the two subevents from the same event are combined, as done in the STAR analysis and also studied in this work, where the squared inverse width of $R_{\Psi_2}(\Delta S'')$ is referred to as ξ , the situation is not clear. If the auto-correlation in Eq. 17 was not considered, then the derivation would also hold for ξ by the same math. In the presence of auto-correlations, however, derivation of a general correction factor may not be possible because it must depend on the nature of those auto-correlations. In the context of our toy model with the RP known, we can use the same resolution scan method described above for ξ_0 and obtain the proper resolution correction factor by ξ_0/ξ_{RP} . This is shown in Fig. 11 as a function of the EP resolution r_2 of subevents. A linear dependence on r_2 is observed, but the intercept is nonzero. The ξ_0/ξ_{RP} is always larger than $\xi_0^*/\xi_{\text{RP}}^*$, and the difference comes from those auto-correlations. See discussion in Sec. 5.1 (cf. Eq. 17) and further discussion in Appendix A.3.

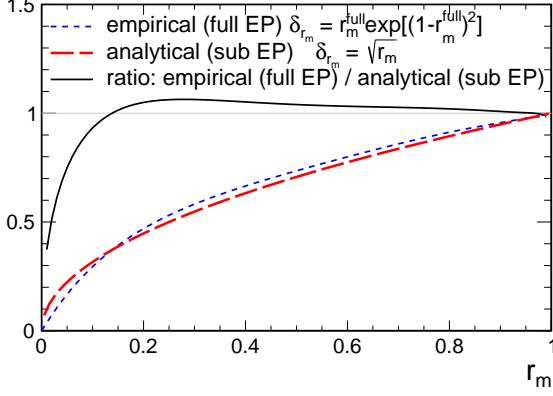


FIG. 12. The analytical and empirical EP resolution correction factors plotted as functions of r_m , the EP resolution of subevents (Eq. 8). The empirical correction factor, used in the STAR paper [21], is calculated from the EP resolution of full events (r_m^{full}), which is a monotonic function of r_m [54]. The ratio of the empirical to analytical correction factors is also shown.

The STAR paper [21] uses an empirical resolution correction factor $\delta_{r_m} = r_m^{\text{full}} e^{(1-r_m^{\text{full}})^2}$, different from our analytical result of Eq. A14. This empirical factor uses the EP resolution of the full event, r_m^{full} , which is a monotonic function of the EP resolution r_m of subevents [54]. At small r_m , $r_m^{\text{full}} \approx \sqrt{2}r_m$. The comparison between them is made in Fig. 12, both plotted as a function of r_m . It is observed that the empirical correction factor is similar to our analytical result of $\sqrt{r_m}$. The ratio of the two is shown by the solid curve in Fig. 12, indicating that the difference is less than 10% in a wide range of resolution ($0.1 < r_m < 1.0$) relevant for our study.

Is the STAR empirical EP resolution correction factor correct? Figure 11 suggests it is not. The correction factors for ξ and ξ^* are clearly different. The difference arises from the auto-correlations of Eq. 17. The STAR empirical correction factor, which is similar to our analytical one, would be approximately correct for ξ^* , but it is incorrect for ξ . In order to compare to the STAR data, we have used our analytical formula to also correct for ξ , which is close to the empirical factor by STAR. The slight difference between the two does not affect our qualitative comparisons to the STAR results.

3. Auto-correlation effect in ξ

As shown in Eq. 17, ξ contains auto-correlations, whereas ξ^* is free of it. In this subsection, we investigate the effect of auto-correlations on ξ . Because the ΔS distributions are even, we have $\langle \Delta S^E \rangle = \langle \Delta S^W \rangle = 0$. The variances of ΔS^E and ΔS^W are equal to their second moments $\text{Var}[\Delta S^E] = \langle (\Delta S^E)^2 \rangle$, $\text{Var}[\Delta S^W] = \langle (\Delta S^W)^2 \rangle$, and the covariance between them is $\text{Cov}[\Delta S^E, \Delta S^W] =$

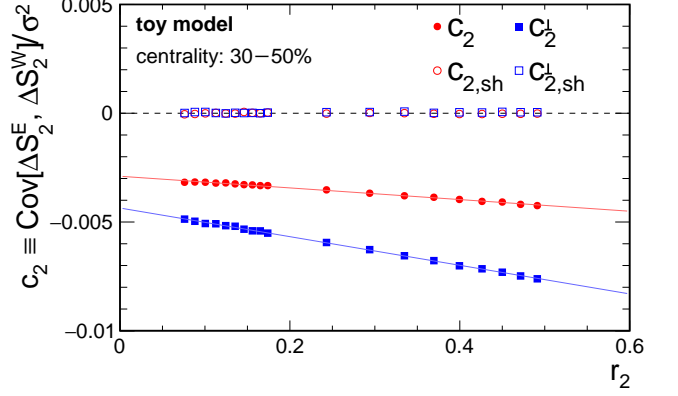


FIG. 13. The correlation factors c as functions of the subevent EP resolution r_2 from the same toy model simulation as Fig. 11. For shuffled charges, the auto-correlations ($c_{2,\text{sh}}$, $c_{2,\text{sh}}^\perp$) vanish. For real charges, the auto-correlations (c_2 , c_2^\perp) are negative, linearly dependent on r_2 , and different between the two directions (parallel or perpendicular to EP). If fitted by straight lines, c_2 and c_2^\perp have discrepancy in their intercepts, which accounts for the nonzero intercept of ξ_0/ξ_{RP} in Fig. 11.

$\langle \Delta S^W \Delta S^E \rangle$. Because the two subevents are symmetric, ΔS^E and ΔS^W should have the same distribution with the same variance $\sigma^2 \equiv \text{Var}[\Delta S^E] = \text{Var}[\Delta S^W]$. For convenience, we call ρ^2 the variance of full-event ΔS defined in Eq. 4. Then, Eq. 17 can be written as

$$\rho^2 = \frac{1}{2}\sigma^2(1+c), \quad (\text{A15})$$

where c is the correlation factor $c \equiv \text{Cov}[\Delta S^E, \Delta S^W]/\sigma^2$. This applies to all four cases (real or shuffled charges, parallel or perpendicular directions).

Figure 13 shows the correlation factors c as functions of the subevent EP resolution r_2 from the same toy model simulation as Fig. 11. For shuffled charges, the auto-correlations ($c_{2,\text{sh}}$, $c_{2,\text{sh}}^\perp$) vanish. For real charges, the auto-correlations (c_2 , c_2^\perp) are negative and linearly dependent on r_2 , but they are different between the two directions (parallel or perpendicular to EP). The auto-correlation factors are quite small, but they have a significant effect on ξ as can be easily seen as follows.

Similar to Eq. A12, we can express ξ_0 by using full-event ΔS width ρ and Eq. A15

$$\begin{aligned} \xi_0 &\equiv - \left(\frac{\rho_{m,\text{sh}}^2}{\rho_m^2} - \frac{\rho_{m,\text{sh}}^{\perp 2}}{\rho_m^{\perp 2}} \right) \\ &\approx - \left(\frac{\sigma_{m,\text{sh}}^2}{\sigma_m^2} (1 - c_m) - \frac{\sigma_{m,\text{sh}}^{\perp 2}}{\sigma_m^{\perp 2}} (1 - c_m^\perp) \right) \\ &\approx - \left(\frac{\sigma_{m,\text{sh}}^2}{\sigma_m^2} - \frac{\sigma_{m,\text{sh}}^{\perp 2}}{\sigma_m^{\perp 2}} \right) + \left(\frac{\sigma_{m,\text{sh}}^2}{\sigma_m^2} + \frac{\sigma_{m,\text{sh}}^{\perp 2}}{\sigma_m^{\perp 2}} \right) \frac{c_m - c_m^\perp}{2}, \end{aligned} \quad (\text{A16})$$

where $m = 2$, and we have used $c_{2,\text{sh}} = c_{2,\text{sh}}^\perp = 0$ and $|c_2|, |c_2^\perp| \ll 1$. If we plug Eq. A5 into the last line, the first term has already been calculated in Eq. A13, which is $\xi_0^* \propto r_m$. The quantity in the second pair of parentheses is

$$\begin{aligned} & \frac{\sigma_{m,\text{sh}}^2}{\sigma_m^2} + \frac{\sigma_{m,\text{sh}}^{\perp 2}}{\sigma_m^{\perp 2}} \\ &= 2 \cdot \frac{(\sigma_\downarrow^2 + \sigma_{\perp\downarrow}^2)(\sigma_\uparrow^2 + \sigma_{\perp\uparrow}^2) - (\sigma_\downarrow^2 - \sigma_{\perp\downarrow}^2)(\sigma_\uparrow^2 - \sigma_{\perp\uparrow}^2)r_m^2}{(\sigma_\uparrow^2 + \sigma_{\perp\uparrow}^2)^2 - (\sigma_\uparrow^2 - \sigma_{\perp\uparrow}^2)^2 r_m^2} \\ &\approx 2 \cdot \frac{\sigma_\downarrow^2 + \sigma_{\perp\downarrow}^2}{\sigma_\uparrow^2 + \sigma_{\perp\uparrow}^2}. \end{aligned} \quad (\text{A17})$$

Thus, Eq. A16 can be written as

$$\xi_0 \approx \xi_0^* + \frac{\sigma_\downarrow^2 + \sigma_{\perp\downarrow}^2}{\sigma_\uparrow^2 + \sigma_{\perp\uparrow}^2} (c_m - c_m^\perp). \quad (\text{A18})$$

The second term is the effect from auto-correlations. Although $(c_2 - c_2^\perp)$ is small, the coefficient in front of it is $\mathcal{O}(1)$, so it has a significant effect on the also-small quantity ξ_0 . It generally also depends on the EP resolution. As shown in Fig. 13, $(c_2 - c_2^\perp)$ is a first-polynomial function of r_2 with a nonzero intercept in our toy model simulation. Was the intercept equal to zero, we would have $\xi_0 \propto r_2$ as well; otherwise ξ_0 linearly depends on r_2 with a finite intercept, as shown in Fig. 11.

In general, auto-correlations should depend on the physics of the particle events. Therefore, there may not be universal resolution correction for ξ . In this work, we have used the same resolution correction factor for both ξ and ξ^* ($\delta_{r_2} = \sqrt{r_2}$), as stated previously, because we want to make the comparison between ξ and ξ^* , and between our analysis and Ref. [21].

Appendix B: Analytical form for ξ^*

In this appendix, we derive analytical forms of ξ^* in the presence of v_2 background and CME signal.

1. Background v_2 dependence

In our previous work [20], we derived the v_2 dependence of $R_{\Psi_2}(\Delta S)$ where ΔS was not scaled. In this section, we derive the v_2 dependence of ξ^* , the squared inverse width of the scaled $R_{\Psi_2}(\Delta S'')$ distribution, where the subevents are treated separately without being averaged. As we mentioned in Sec. 5.1, the averaging introduces auto-correlations which make the analytical derivation inexplicable.

We only focus on the primordial pions (n_π) and the daughter pions from ρ resonance decays (n_ρ). The CME signal is fixed to be zero (i.e. $a_1 = 0$). We assume that

the number of π^+ and π^- are the same ($n_{\pi^+} = n_{\pi^-} = n_\pi/2$), and denote the elliptic flow coefficients as $v_{2,\pi}$ for primordial pions and $v_{2,\rho}$ for ρ mesons.

The analysis based on the central limit theorem (CLT) [20] tells us that the widths for $\Delta S_2(\Psi_{\text{RP}})$, $\Delta S_2^\perp(\Psi_{\text{RP}})$, $\Delta S_{2,\text{sh}}(\Psi_{\text{RP}})$, $\Delta S_{2,\text{sh}}^\perp(\Psi_{\text{RP}})$ are

$$\begin{aligned} \sigma_\uparrow^2 &= \frac{n_\rho K(1 + v_{2,\rho}) + n_\pi(1 - v_{2,\pi})}{2(n_\rho + 0.5n_\pi)^2} \\ \sigma_{\perp\uparrow}^2 &= \frac{n_\rho K(1 - v_{2,\rho}) + n_\pi(1 + v_{2,\pi})}{2(n_\rho + 0.5n_\pi)^2} \\ \sigma_\downarrow^2 &= \frac{2n_\rho(1 - v_{2,\rho}) + n_\rho v_{2,\rho} K + n_\pi(1 - v_{2,\pi})}{2(n_\rho + 0.5n_\pi)^2} \\ \sigma_{\perp\downarrow}^2 &= \frac{2n_\rho(1 + v_{2,\rho}) - n_\rho v_{2,\rho} K + n_\pi(1 + v_{2,\pi})}{2(n_\rho + 0.5n_\pi)^2}, \end{aligned} \quad (\text{B1})$$

where $K = \text{Var}[2\sin(\delta\phi/2)]$ is the variance of the sine value of the half decay opening angle ($\delta\phi = \phi_+ - \phi_-$, with ϕ_+ and ϕ_- being the azimuths of the π^+ and π^- from the same ρ decay). Similar to Eq. A11, the observable ξ^* , in which only background is present in the current case, is

$$\begin{aligned} \xi_{\text{bkgd}}^* &= -\frac{\sigma_\downarrow^2}{\sigma_\uparrow^2} + \frac{\sigma_{\perp\downarrow}^2}{\sigma_{\perp\uparrow}^2} \\ &= \frac{\alpha\beta K(4 - K) + (K + 2\beta - 2)}{(\alpha K + 1)^2 - (\alpha K\beta - 1)^2 v_{2,\pi}^2} \times 2\alpha v_{2,\pi}, \end{aligned} \quad (\text{B2})$$

where $\alpha = n_\rho/n_\pi$ and $\beta = v_{2,\rho}/v_{2,\pi}$. Since $v_{2,\pi} \ll 1$, the second term in the denominator of Eq. B2 can be safely neglected. We thus have

$$\xi_{\text{bkgd}}^* \approx \frac{\alpha\beta K(4 - K) + (K + 2\beta - 2)}{(\alpha K + 1)^2} \times 2\alpha v_{2,\pi}. \quad (\text{B3})$$

We can see that, for pure background, ξ^* is approximately proportional to the background v_2 .

In our toy model simulations, the multiplicity ratio of ρ to primordial pions is 0.085. To have a rough estimate, we can take $\alpha = 0.085$. The $v_{2,\rho}$ is parameterized taking into account the NCQ scaling at high p_T and the hydrodynamics mass ordering of v_2 at low p_T ; we find $\beta \approx 1.1$. From our previous study, we found the RMS of $2\sin(\delta\phi/2)$ is 1.36 [20], thus $K = 1.36^2 = 1.85$. With these estimates of α, β, K , we have

$$\xi_{\text{bkgd}}^* \approx 0.31 v_{2,\pi}. \quad (\text{B4})$$

This is about a factor of 3 larger compared to our toy model simulation in Sec. 5.1 (cf. Eq. 18b). In our derivation here, we have simply assumed that all ρ decay daughters are included in the POI's. In the toy model using subevents, only a fraction of the ρ resonances have both daughters in the subevent acceptance. This would significantly reduce the coefficient in the toy model compared to the derivation in Eq. B3. Other simplifying assumptions, such as neglecting correlations arising from p_T dependence of v_2 and decay kinematics, may also contribute

to the numerical difference. However, the qualitative features in the results from the analytical derivation, namely the proportionality to v_2 and the N_{ch} independence, are robust and provide useful insights.

2. Signal a_1 dependence

In this section, we derive analytically the dependence of ξ^* on the CME signal strength, a_1 . The primordial particle a_1 in Eq. 1 is nonzero for each event, but it can be either positive or negative for different events, so the event average of a_1 is still zero. On one hand, the positive and negative charges in the same event always have opposite a_1 , so shuffling the charges removes the signal contribution. On the other hand, the signal only contributes to the charge separation in the y -direction, so the x -projection is not affected. Thus, only the distribution of ΔS_m has dependence on a_1 . In this section, we will only focus on the second-order ΔS_2 with respect to RP, namely

$$\Delta S = \frac{1}{n^+} \sum_i^{n^+} \sin(\phi_i^+ - \Psi_{RP}) - \frac{1}{n^-} \sum_i^{n^-} \sin(\phi_i^- - \Psi_{RP}), \quad (\text{B5})$$

where we assume $n^+ = n^- = 0.5n_\pi + n_\rho$ as mentioned in Appendix B.1.

We first fix a_1 and get the conditional expectation and variance of ΔS . It is straightforward that the average of $\pm \sin(\phi^\pm - \Psi_{RP})$ over all primordial particles among all events is

$$\text{E} [\pm \sin(\phi^\pm - \Psi_{RP}) | a_1] = a_1, \quad (\text{B6})$$

and the conditional variance is

$$\begin{aligned} & \text{Var} [\pm \sin(\phi^\pm - \Psi_{RP}) | a_1] \\ &= \langle \sin^2(\phi^\pm - \Psi_{RP}) \rangle - \langle \pm \sin(\phi^\pm - \Psi_{RP}) \rangle^2 \\ &= \frac{1 - v_{2,\pi} - 2a_1^2}{2}. \end{aligned} \quad (\text{B7})$$

Thus, we can get the conditional variance of ΔS by substituting $v_{2,\pi}$ by $v_{2,\pi} + 2a_1^2$ for σ_\uparrow^2 in the first line of Eq. B1, namely

$$\text{Var} [\Delta S | a_1] = \frac{n_\rho K(1 + v_{2,\rho}) + n_\pi(1 - v_{2,\pi} - 2a_1^2)}{2(n_\rho + 0.5n_\pi)^2}. \quad (\text{B8})$$

We can also get the conditional expectation of ΔS

$$\text{E} [\Delta S | a_1] = \frac{n_\pi}{0.5n_\pi + n_\rho} a_1. \quad (\text{B9})$$

Now with varying a_1 from event to event, since the topologic charge fluctuation is totally random among events, a_1 is a symmetric distribution about 0, so

$\text{Var} [a_1] = \langle a_1^2 \rangle$. Thus, the total variance can be calculated

$$\begin{aligned} & \sigma_\uparrow^2(\langle a_1^2 \rangle) = \text{Var} [\Delta S] \\ &= \text{E} [\text{Var} [\Delta S | a_1]] + \text{Var} [\text{E} [\Delta S | a_1]] \\ &\approx \frac{n_\rho K(1 + v_{2,\rho}) + n_\pi(1 - v_{2,\pi} - 2\langle a_1^2 \rangle)}{2(n_\rho + 0.5n_\pi)^2} \\ &\quad + \left(\frac{n_\pi}{0.5n_\pi + n_\rho} \right)^2 \langle a_1^2 \rangle \\ &\approx \sigma_\uparrow^2(0) + \left(\frac{n_\pi}{0.5n_\pi + n_\rho} \right)^2 \langle a_1^2 \rangle, \end{aligned} \quad (\text{B10})$$

where we have assumed $v_{2,\pi} \gg a_1^2$ so the latter is dropped from the first term, which is then simply given by Eq. B1 without the a_1 signal.

Again, for convenience, we write all ΔS distributions as Gaussians, Eq. B2 would be modified, with finite a_1 , into

$$\begin{aligned} & \xi^*(\langle a_1^2 \rangle) = -\frac{\sigma_\downarrow^2}{\sigma_\uparrow^2(\langle a_1^2 \rangle)} + \frac{\sigma_{\perp\downarrow}^2}{\sigma_{\perp\uparrow}^2} \\ &= -\frac{\sigma_\downarrow^2}{\sigma_\uparrow^2(0)} \left(1 + \left(\frac{n_\pi}{0.5n_\pi + n_\rho} \right)^2 \frac{\langle a_1^2 \rangle}{\sigma_\uparrow^2(0)} \right)^{-1} + \frac{\sigma_{\perp\downarrow}^2}{\sigma_{\perp\uparrow}^2} \\ &\approx -\frac{\sigma_\downarrow^2}{\sigma_\uparrow^2(0)} + \frac{\sigma_{\perp\downarrow}^2}{\sigma_{\perp\uparrow}^2} + \left(\frac{n_\pi}{0.5n_\pi + n_\rho} \right)^2 \frac{\sigma_\downarrow^2}{\sigma_\uparrow^4(0)} \langle a_1^2 \rangle \\ &\approx \xi_{\text{bkgd}}^* + 2N_{ch}(1 + v_{2,\pi} - 2\alpha K) \langle a_1^2 \rangle, \end{aligned} \quad (\text{B11})$$

where the first term, ξ_{bkgd}^* , is that given by Eq. B3 without a_1 signal. The first approximation comes from the fact that $\sigma_\uparrow^2(0) \gg \langle a_1^2 \rangle$, as $\sigma_\uparrow^2(0) \sim 1/n_\pi \sim 10^{-2}$ and $\langle a_1^2 \rangle \sim 10^{-4}$. We simply take the number of POI's as $N_{ch} \approx n_\pi + 2n_\rho$. We can see from Eq. B11 that the background and the CME are approximately decoupled in ξ^* , and the CME signal $\xi^*(\langle a_1^2 \rangle)$ has linear dependence on $\langle a_1^2 \rangle$.

With the aforementioned values for α and K , we can estimate the signal contribution to be

$$\xi_{\text{CME}}^* \approx 1.49 \langle a_1^2 \rangle N_{ch}. \quad (\text{B12})$$

This is close to the toy model simulation result in Eq. 20b. The S/B of $\xi^*(\langle a_1^2 \rangle)$ can be estimated as

$$S/B = \frac{1.49 \langle a_1^2 \rangle N_{ch}}{0.34 v_{2,\pi}} = 4.8 \langle a_1^2 \rangle N_{ch} / v_{2,\pi}, \quad (\text{B13})$$

which is about a factor of 3 smaller than the toy model result of Eq. 21b, mainly inherited from the discrepancy in ξ_{bkgd}^* estimation in Appendix B.1.

Appendix C: Analytical form for $\Delta\gamma$

For completeness, we can easily obtain $\Delta\gamma$ from Eqs. 12-14.

$$\begin{aligned}\Delta\gamma &\approx \frac{n_\rho}{(n_\pi/2 + n_\rho)^2} v_{2,\rho} D + 2 \left(\frac{n_\pi/2}{n_\rho + n_\pi/2} \right)^2 \langle a_1^2 \rangle \\ &= \frac{4\alpha D \beta}{1 + 2\alpha} \frac{v_{2,\pi}}{N_{ch}} + \frac{2}{(1 + 2\alpha)^2} \langle a_1^2 \rangle,\end{aligned}\quad (\text{C1})$$

where $D = \langle \cos(\phi_a + \phi_b - 2\phi_{\text{reso}}) \rangle$ as shown in Eq. 14. Taking $D \sim 0.65$ [32] and the aforementioned α and β values, we obtain $\Delta\gamma$ for our toy model setting in this work as

$$\Delta\gamma \approx 0.21 v_{2,\pi} / N_{ch} + 1.46 \langle a_1^2 \rangle. \quad (\text{C2})$$

The S/B for $\Delta\gamma$ is then

$$\begin{aligned}\frac{n_\pi^2}{2n_\rho} \frac{\langle a_1^2 \rangle}{v_{2,\rho} D} &= \frac{1}{2\alpha(1 + 2\alpha)\beta D} N_{ch} \langle a_1^2 \rangle / v_{2,\pi} \\ &\approx 7.0 N_{ch} \langle a_1^2 \rangle / v_{2,\pi}.\end{aligned}\quad (\text{C3})$$

The proportionality coefficient on a_1^2 is close to that obtained from our toy model simulation in Eq. 20c. The coefficient on the v_2 background is about a factor of 2 larger than that from the toy model simulation. This arises from similar reasons responsible for the discrepancy in ξ_{bkgd}^* between the analytical estimate and the toy model simulation. Namely, not all ρ resonances have both decay daughters in the subevent acceptance, and correlations exist among various quantities because of their dependences on p_T . Note that those effects appear to yield a larger discrepancy in ξ^* than in $\Delta\gamma$. As a result, the S/B seems better for ξ^* than $\Delta\gamma$ in our toy model simulation, and it is reversed in the analytical results. This quantitative feature likely depends on the details of the model implementation, such as the types of resonances included and their abundances.

-
- [1] T. Lee and G. Wick, Vacuum stability and vacuum excitation in a spin 0 field theory, *Phys.Rev.* **D9**, 2291 (1974).
- [2] P. D. Morley and I. A. Schmidt, Strong P, CP, T violations in heavy ion collisions, *Z. Phys.* **C26**, 627 (1985).
- [3] D. Kharzeev, R. Pisarski, and M. H. Tytgat, Possibility of spontaneous parity violation in hot QCD, *Phys.Rev.Lett.* **81**, 512 (1998), arXiv:hep-ph/9804221 [hep-ph].
- [4] D. E. Kharzeev, L. D. McLerran, and H. J. Warringa, The Effects of topological charge change in heavy ion collisions: 'Event by event P and CP violation', *Nucl.Phys.* **A803**, 227 (2008), arXiv:0711.0950 [hep-ph].
- [5] S. A. Voloshin, Parity violation in hot QCD: How to detect it, *Phys.Rev.* **C70**, 057901 (2004), arXiv:hep-ph/0406311 [hep-ph].
- [6] B. Abelev *et al.* (STAR Collaboration), Azimuthal Charged-Particle Correlations and Possible Local Strong Parity Violation, *Phys.Rev.Lett.* **103**, 251601 (2009), arXiv:0909.1739 [nucl-ex].
- [7] B. Abelev *et al.* (STAR Collaboration), Observation of charge-dependent azimuthal correlations and possible local strong parity violation in heavy ion collisions, *Phys.Rev.* **C81**, 054908 (2010), arXiv:0909.1717 [nucl-ex].
- [8] L. Adamczyk *et al.* (STAR), Beam-energy dependence of charge separation along the magnetic field in Au+Au collisions at RHIC, *Phys. Rev. Lett.* **113**, 052302 (2014), arXiv:1404.1433 [nucl-ex].
- [9] L. Adamczyk *et al.* (STAR), Fluctuations of charge separation perpendicular to the event plane and local parity violation in $\sqrt{s_{NN}} = 200$ GeV Au+Au collisions at the BNL Relativistic Heavy Ion Collider, *Phys. Rev.* **C88**, 064911 (2013), arXiv:1302.3802 [nucl-ex].
- [10] J. Zhao (STAR), Chiral magnetic effect search in p+Au, d+Au and Au+Au collisions at RHIC, *Proceedings, 47th International Symposium on Multiparticle Dynamics (ISMD2017): Tlaxcala, Tlaxcala, Mexico, September 11-15, 2017*, EPJ Web Conf. **172**, 01005 (2018), arXiv:1712.00394 [hep-ex].
- [11] J. Zhao (STAR), Charge dependent particle correlations motivated by chiral magnetic effect and chiral vortical effect, *Proceedings, 46th International Symposium on Multiparticle Dynamics (ISMD 2016): Jeju Island, South Korea, August 29-September 2, 2016*, EPJ Web Conf. **141**, 01010 (2017).
- [12] B. Abelev *et al.* (ALICE), Charge separation relative to the reaction plane in Pb-Pb collisions at $\sqrt{s_{NN}} = 2.76$ TeV, *Phys.Rev.Lett.* **110**, 012301 (2013), arXiv:1207.0900 [nucl-ex].
- [13] V. Khachatryan *et al.* (CMS), Observation of charge-dependent azimuthal correlations in p-Pb collisions and its implication for the search for the chiral magnetic effect, *Phys. Rev. Lett.* **118**, 122301 (2017), arXiv:1610.00263 [nucl-ex].
- [14] A. M. Sirunyan *et al.* (CMS), Constraints on the chiral magnetic effect using charge-dependent azimuthal correlations in pPb and PbPb collisions at the CERN Large Hadron Collider, *Phys. Rev. C* **97**, 044912 (2018), arXiv:1708.01602 [nucl-ex].
- [15] S. Acharya *et al.* (ALICE), Constraining the magnitude of the Chiral Magnetic Effect with Event Shape Engineering in Pb-Pb collisions at $\sqrt{s_{NN}} = 2.76$ TeV, *Phys. Lett.* **B777**, 151 (2018), arXiv:1709.04723 [nucl-ex].
- [16] S. Acharya *et al.* (ALICE), Constraining the Chiral Magnetic Effect with charge-dependent azimuthal correlations in Pb-Pb collisions at $\sqrt{s_{NN}} = 2.76$ and 5.02 TeV, *JHEP* **09**, 160, arXiv:2005.14640 [nucl-ex].
- [17] N. Ajitanand, R. A. Lacey, A. Taranenko, and J. Alexander, A New method for the experimental study of topological effects in the quark-gluon plasma, *Phys.Rev.* **C83**, 011901 (2011), arXiv:1009.5624 [nucl-ex].
- [18] N. Magdy, S. Shi, J. Liao, N. Ajitanand, and R. A. Lacey, A new correlator to detect and characterize the

- chiral magnetic effect, Phys. Rev. **C97**, 061901 (2018), arXiv:1710.01717 [physics.data-an].
- [19] P. Bożek, Azimuthal angle dependence of the charge imbalance from charge conservation effects, Phys. Rev. C **97**, 034907 (2018), arXiv:1711.02563 [nucl-th].
- [20] Y. Feng, J. Zhao, and F. Wang, Responses of the chiral-magnetic-effect-sensitive sine observable to resonance backgrounds in heavy-ion collisions, Phys. Rev. C **98**, 034904 (2018), arXiv:1803.02860 [nucl-th].
- [21] J. Adam *et al.* (STAR), Charge separation measurements in $p(d)+au$ and $au+au$ collisions; implications for the chiral magnetic effect, (2020), arXiv:2006.04251.
- [22] Z.-W. Lin, C. M. Ko, B.-A. Li, B. Zhang, and S. Pal, A Multi-phase transport model for relativistic heavy ion collisions, Phys.Rev. **C72**, 064901 (2005), arXiv:nucl-th/0411110 [nucl-th].
- [23] Y. Jiang, S. Shi, Y. Yin, and J. Liao, Quantifying the chiral magnetic effect from anomalous-viscous fluid dynamics, Chinese Physics C **42**, 011001 (2018), arXiv:1611.04586.
- [24] S. Shi, Y. Jiang, E. Lilleskov, and J. Liao, Anomalous Chiral Transport in Heavy Ion Collisions from Anomalous-Viscous Fluid Dynamics, Annals of Physics **394**, 50 (2018), arXiv:1711.02496 [nucl-th].
- [25] J. Schukraft, A. Timmins, and S. A. Voloshin, Ultra-relativistic nuclear collisions: event shape engineering, Phys. Lett. **B719**, 394 (2013), arXiv:1208.4563 [nucl-ex].
- [26] F. Wang, Effects of Cluster Particle Correlations on Local Parity Violation Observables, Phys.Rev. **C81**, 064902 (2010), arXiv:0911.1482 [nucl-ex].
- [27] L. Adamczyk *et al.* (STAR), Measurement of charge multiplicity asymmetry correlations in high-energy nucleus-nucleus collisions at $\sqrt{s_{NN}} = 200$ GeV, Phys. Rev. **C89**, 044908 (2014), arXiv:1303.0901 [nucl-ex].
- [28] A. Bzdak, V. Koch, and J. Liao, Remarks on possible local parity violation in heavy ion collisions, Phys.Rev. **C81**, 031901 (2010), arXiv:0912.5050 [nucl-th].
- [29] S. Schlichting and S. Pratt, Charge conservation at energies available at the BNL Relativistic Heavy Ion Collider and contributions to local parity violation observables, Phys.Rev. **C83**, 014913 (2011), arXiv:1009.4283 [nucl-th].
- [30] N. Magdy, M.-W. Nie, G.-L. Ma, and R. A. Lacey, A sensitivity study of the primary correlators used to characterize chiral-magnetically-driven charge separation, Physics Letters B **809**, 135771 (2020), arXiv:2002.07934.
- [31] Y. Feng, F. Wang, and J. Zhao, Comment on "a sensitivity study of the primary correlators used to characterize chiral-magnetically-driven charge separation" by magdy, nie, ma, and lacey (2020), arXiv:2009.10057.
- [32] F. Wang and J. Zhao, Challenges in flow background removal in search for the chiral magnetic effect, Phys. Rev. **C95**, 051901 (2017), arXiv:1608.06610 [nucl-th].
- [33] J. Adams *et al.* (STAR), ρ_0 production and possible modification in Au+Au and p+p collisions at $S(NN)^{1/2} = 200$ -GeV, Phys. Rev. Lett. **92**, 092301 (2004), arXiv:nucl-ex/0307023 [nucl-ex].
- [34] S. Adler *et al.* (PHENIX Collaboration), Suppressed π^0 production at large transverse momentum in central Au+Au collisions at $S(NN)^{1/2} = 200$ GeV, Phys.Rev.Lett. **91**, 072301 (2003), arXiv:nucl-ex/0304022 [nucl-ex].
- [35] J. Adams *et al.* (STAR), Identified particle distributions in pp and Au+Au collisions at $s(NN)^{1/2} = 200$ GeV, Phys. Rev. Lett. **92**, 112301 (2004), arXiv:nucl-ex/0310004 [nucl-ex].
- [36] B. Abelev *et al.* (STAR Collaboration), Systematic measurements of identified particle spectra in pp, d+Au and Au+Au collisions from STAR, Phys.Rev. **C79**, 034909 (2009), arXiv:0808.2041 [nucl-ex].
- [37] J. Adams *et al.* (STAR Collaboration), Azimuthal anisotropy in Au+Au collisions at $s(NN)^{1/2} = 200$ -GeV, Phys.Rev. **C72**, 014904 (2005), arXiv:nucl-ex/0409033 [nucl-ex].
- [38] A. Adare *et al.* (PHENIX), Azimuthal anisotropy of neutral pion production in Au+Au collisions at $\sqrt{s_{NN}} = 200$ GeV: Path-length dependence of jet quenching and the role of initial geometry, Phys. Rev. Lett. **105**, 142301 (2010), arXiv:1006.3740 [nucl-ex].
- [39] X. Dong, S. Esumi, P. Sorensen, N. Xu, and Z. Xu, Resonance decay effects on anisotropy parameters, Phys. Lett. **B597**, 328 (2004), arXiv:nucl-th/0403030 [nucl-th].
- [40] L. Adamczyk *et al.* (STAR), Measurements of Dielectron Production in Au+Au Collisions at $\sqrt{s_{NN}} = 200$ GeV from the STAR Experiment, Phys. Rev. **C92**, 024912 (2015), arXiv:1504.01317 [hep-ex].
- [41] K. A. Olive *et al.* (Particle Data Group), Review of Particle Physics, Chin. Phys. **C38**, 090001 (2014).
- [42] B. Abelev *et al.* (STAR Collaboration), Studying Parton Energy Loss in Heavy-Ion Collisions via Direct-Photon and Charged-Particle Azimuthal Correlations, Phys.Rev. **C82**, 034909 (2010), arXiv:0912.1871 [nucl-ex].
- [43] Sergei A. Voloshin, private communication.
- [44] Aihong Tang, Prithwish Tribedy, and Gang Wang, private communications.
- [45] Nanxi Yao, Method study of azimuthal correlators in search of the chiral magnetic effect in heavy-ion collisions (2020), Fall Meeting of the APS Division of Nuclear Physics.
- [46] J. Zhao, H. Li, and F. Wang, Isolating the chiral magnetic effect from backgrounds by pair invariant mass, Eur. Phys. J. C **79**, 168 (2019), arXiv:1705.05410 [nucl-ex].
- [47] H. Li, J. Zhao, and F. Wang, A novel invariant mass method to isolate resonance backgrounds from the chiral magnetic effect, Nucl. Phys. A **982**, 563 (2019), arXiv:1808.03210 [nucl-ex].
- [48] J. Zhao (STAR), Measurements of the chiral magnetic effect with background isolation in 200 GeV Au+Au collisions at STAR, Nucl. Phys. A **982**, 535 (2019), arXiv:1807.09925 [nucl-ex].
- [49] H.-J. Xu, J. Zhao, X.-B. Wang, H.-L. Li, Z.-W. Lin, C.-W. Shen, and F.-Q. Wang, Varying the chiral magnetic effect relative to flow in a single nucleus-nucleus collision, Chinese Physics C **42**, 084103 (2018), arXiv:1710.07265 [nucl-th].
- [50] H.-j. Xu, J. Zhao, X. Wang, H. Li, Z.-W. Lin, C. Shen, and F. Wang, Re-examining the premise of isobaric collisions and a novel method to measure the chiral magnetic effect, Nucl. Phys. A **982**, 531 (2019), arXiv:1808.00133 [nucl-th].
- [51] J. Zhao (STAR), Search for CME in U+U and Au+Au collisions in STAR with different approaches of handling backgrounds, Nucl. Phys. A **1005**, 121766 (2021), arXiv:2002.09410 [nucl-ex].
- [52] H.-j. Xu, X. Wang, H. Li, J. Zhao, Z.-W. Lin, C. Shen, and F. Wang, Importance of isobar density distributions on the chiral magnetic effect search, Phys. Rev. Lett.

- 121**, 022301 (2018), arXiv:1710.03086 [nucl-th].
- [53] N. Magdy, S. Shi, J. Liao, P. Liu, and R. A. Lacey, Examination of the observability of a chiral magnetically driven charge-separation difference in collisions of the ${}^{96}_{44}\text{Ru} + {}^{96}_{44}\text{Ru}$ and ${}^{96}_{40}\text{Zr} + {}^{96}_{40}\text{Zr}$ isobars at energies available at the bnl relativistic heavy ion collider, Phys. Rev. C **98**, 061902 (2018).
- [54] A. M. Poskanzer and S. Voloshin, Methods for analyzing anisotropic flow in relativistic nuclear collisions, Phys.Rev. **C58**, 1671 (1998), arXiv:nucl-ex/9805001 [nucl-ex].